creative commons

COMMONS DEED

저작자표시-비영리-변경금지 2.0 대한민국

이용자는 아래의 조건을 따르는 경우에 한하여 자유롭게

- 이 저작물을 복제, 배포, 전송, 전시, 공연 및 방송할 수 있습니다.

다음과 같은 조건을 따라야 합니다:

**저작자표시.** 귀하는 원저작자를 표시하여야 합니다.

**비영리.** 귀하는 이 저작물을 영리 목적으로 이용할 수 없습니다.

**변경금지.** 귀하는 이 저작물을 개작, 변형 또는 가공할 수 없습니다.

- 귀하는, 이 저작물의 재이용이나 배포의 경우, 이 저작물에 적용된 이용허락조건을 명확하게 나타내어야 합니다.
- 저작권자로부터 별도의 허가를 받으면 이러한 조건들은 적용되지 않습니다.

**저작권법에 따른 이용자의 권리는 위의 내용에 의하여 영향을 받지 않습니다.**

이것은 이용허락규약(Legal Code)을 이해하기 쉽게 요약한 것입니다.

Disclaimer

dCollection

Ph.D. DISSERTATION

# A Study on Channel Prediction and Positioning Techniques for Beyond 5G Communications Systems

## Beyond 5G 통신 시스템을 위한 채널 예측 및 위치 추정 기법 연구

BY

LEE JUNG-YONG

AUGUST 2019

DEPARTMENT OF ELECTRICAL ENGINEERING AND COMPUTER SCIENCE
COLLEGE OF ENGINEERING
SEOUL NATIONAL UNIVERSITY

Ph.D. DISSERTATION

# A Study on Channel Prediction and Positioning Techniques for Beyond 5G Communications Systems

## Beyond 5G 통신 시스템을 위한 채널 예측 및 위치 추정 기법 연구

BY

LEE JUNG-YONG

AUGUST 2019

DEPARTMENT OF ELECTRICAL ENGINEERING AND COMPUTER SCIENCE
COLLEGE OF ENGINEERING
SEOUL NATIONAL UNIVERSITY

# A Study on Channel Prediction and Positioning Techniques for Beyond 5G Communications Systems

## Beyond 5G 통신 시스템을 위한 채널 예측 및 위치 추정 기법 연구

지도교수 김 성 철

이 논문을 공학박사 학위논문으로 제출함

2019년 8월

서울대학교 대학원

전기 컴퓨터 공학부

이 정 용

이정용의 공학박사 학위 논문을 인준함

2019년 8월

위 원 장: ______________________________
부위원장: ______________________________
위 원: ______________________________
위 원: ______________________________
위 원: ______________________________

# Abstract

Recently, to cope with rapidly increasing data traffic, ITU-R established the concept of 5th generation mobile communication (5G) and defined requirements. Additionally, the 3GPP group has developed a new radio (NR) standard for 5G use, and the 5G era has opened in Korea. Unlike current mobile telecommunication systems, the 5G mobile telecommunication system has high speed, ultra-low delay, super-connected characteristics, and it is planned to be used for IoT. Also, the 5G will use the millimeter-wave band as an approach for ultra-high speed communication. The millimeter-wave band uses a wide frequency band. Thus, high data rates can be achieved. However, high path loss, attenuation due to diffraction, etc. are significant challenges in using the millimeter-wave. It is necessary to study the propagation characteristics of waves in detail to utilize the millimeter-wave in a communication system. In particular, to represent the millimeter-wave characteristic in which the attenuation due to diffraction and transmission is very intense, it is necessary to analyze the influence of various obstacles on the millimeter-wave propagation characteristic. Also, the 5G system considers the base station that can move to flexibly cope with the increasing data traffic and the disaster situation. Fast and accurate channel analysis and coverage prediction are essential for mobile base stations, such as drones. The 5G and beyond system, meanwhile, plans to utilize the IoT platform actively. Estimating the location of devices is an essential aspect of increasing the practicality of IoT platforms. In this thesis, I present techniques for resolving various issues that the beyond 5G system faces.

First, I proposed a method for improving the ranging performance for the localization using orthogonal frequency-division multiplexing-based communication system. The most difficult aspect of performing localization using the time-of-arrival information of a communication system is distinguishing indirect paths and noise from the direct path (DP) when the DP is blocked by obstacles. The combination of interference cancellation and an enhanced path detector is proposed to remove interference from nearby paths and detect low power DP. The proposed method is verified in 802.11ac environments, and it shows improved performance compared to conventional methods.

Next, I model roadside trees using a variety of techniques to analyze their effect on the accuracy of channel modeling using ray tracing simulation. The roadside trees were modeled as objects transmitting, reflecting, and diffracting electromagnetic waves. I noted that the results of ray tracing simulations that included roadside trees were more accurate than simulations without tree effects, based on the deviations from the experimentally measured results.

Finally, I propose a new algorithm for predicting the path loss exponent of outdoor millimeter-wave band channels through deep learning method. The proposed algorithm has the advantage of requiring less inference time compared to existing deterministic channel models while concretely considering the topographical characteristics. I used three-dimensional ray tracing to generate the outdoor millimeter-wave band channel and path loss exponent. I trained a neural network with generated path loss exponent. To evaluate the performance of the proposed method, I analyzed the influence of the hyperparameters and environmental features, for example, building density and average distance from the transmitter.

**keywords**: Channel modeling, deep learning, direct path, localization, millimeter wave, orthogonal frequency-division multiplexing, path loss exponent, ray tracing, vegetation.

**student number**: 2013-20856

# Contents

# List of Tables

# List of Figures

# Chapter 1

# INTRODUCTION

Recently, the fifth generation (5G) mobile communication system has been adopted around the world. In 2015, the ITU-R sub-organization Working Party 5D (WP 5D) presented the target performance and service scenarios of 5G. The 5G system requires a substantially more advanced level of technology than 4G in quantitative terms, such as ensuring maximum transmission speeds of 20 Gbps, ensuring that user plane delays are less than 1 ms, and supporting $10^6$ wireless connections per unit $\mathrm{km}^2$. Based on these requirements, ITU-R presented three service scenarios that represent 5G systems: enhanced broadband (eMBB), ultra reliable low latency communications (URLLC), and massive macro communications (mMTC). eMBB, which is an ultra-wide-band mobile data service, is expected to provide new application services such as UHD video streaming, VR, AR and hologram. URLLC is an ultra-reliable low latency communication service that can be used for autonomous driving, care, etc. mMTC, a large-scale object-communication service, is expected to provide a communication platform for the efficient operation of numerous IoT devices. However, it is essential to accurately analyze the channel characteristics of the 5G communication system to provide a service that is far superior in comparison with existing communication systems. Furthermore, for the effective operation of IoT devices, it is necessary to study the method of determining the location of these devices based on the analysis of the channel characteristics of the communication system. Thus, I will examine the three major issues relating to a beyond 5G communication system for my dissertation topic.

The first issue is about the technique of accurately locating mobile devices in a variety of environments, including the NLOS environment. A method for improving the ranging performance for the localization using orthogonal frequency-division multiplexing-based communication system is proposed in this chapter. The most difficult aspect of performing localization using the time-of-arrival information of a communication system is distinguishing indirect paths and noise from the direct path (DP) when the DP is blocked by obstacles. In this chapter, the combination of interference cancellation and an enhanced path detector is proposed to remove interference from nearby paths and detect low power DP. The proposed method is verified in 802.11ac environments, and it shows improved performance compared to conventional methods.

The second issue is about, channel measurement and modeling considering the surrounding environment. To be specific, I modeled roadside trees using a variety of techniques to analyze their effect on the accuracy of channel modeling using ray tracing simulation. The roadside trees were modeled as objects transmitting, reflecting, and diffracting electromagnetic waves. I used a database of roadside trees recorded through the analysis of street view and satellite map data, in combination with a commercially available building database, to perform ray tracing simulations. In this chapter, I've noted that the results of ray tracing simulations that included roadside trees were more accurate than simulations without tree effects, based on the deviations from the experimentally measured results. Also, I studied the influence of a variety of roadside tree models using path loss and multipath component analysis. The improved prediction accuracy highlighted the influence of the inclusion of roadside trees in modeling millimeter wave channels. I also noted differences in the accuracy of the predicted channel depending on the tree modeling method.

Finally, methods using deep learning techniques were studied for quick and accurate channel predictions. In the existing 3G and 4G communication systems, the computational complexity, inference time, and accuracy of the channel models were not the biggest issue because there was little need for an accurate and rapid prediction of the optimum location of the base station. However, with the arrival of 5G communication and the need for smaller coverage and moving base stations like drone-base stations, the task of finding the optimal location of the base station is common and must be done in a very short time. In this chapter, I proposed a new algorithm for predicting the path loss exponent of outdoor millimeter-wave band channels through deep learning method. The proposed algorithm has the advantage of requiring less inference time compared to existing deterministic channel models while concretely considering the topographical characteristics. I used three-dimensional ray tracing to generate the outdoor millimeter-wave band channel and path loss exponent. I trained a neural network with generated path loss exponent. To evaluate the performance of the proposed method, I analyzed the influence of the hyperparameters and environmental features, for example, building density and the average distance from the transmitter.

# Chapter 2

# Enhanced Path Detection based on Undesired Leakage Cancellation for Range Estimation of Communication-based Positioning System in Indoor Environment

## 2.1 Motivation

Recently, there has been an increasing interest in indoor positioning techniques, which are essential for the internet of things devices and systems. Unlike localization technologies that use sensors such as global positioning systems and cameras, when communication systems such as wireless local area networks or cellular networks are used for positioning, no additional equipment is required. However, because the channel of a wireless communication system is significantly influenced by the surrounding environment, the performance of localization using the communication system is greatly affected by the surroundings, such as obstacles between the transceivers. When performing positioning, it is essential to estimate the length of the direct path (DP), which is a straight line connecting the transceivers. The length of the DP can be measured using various parameters, such as the received signal strength, the angle of arrival, and the time of arrival (ToA). In particular, when ToA is used, the length of the DP can be obtained by multiplying the ToA with the speed of light. However, it should be noted that when the line-of-sight (LOS) is blocked by an obstacle, a path other than the DP can be mistaken as the shortest path. The difference in distance between the two paths causes a significant range error, which degrades the positioning performance.

Recently, some studies have been conducted to identify ToAs in communication systems [1, 2, 3, 4, 5, 11, 12, 13, 14, 8, 9, 10, 6, 7, 15, 16, 17, 18, 19]. Nevertheless, few studies have focused on solving cases where obstacles significantly reduced the power of DP. The study of [1, 2, 3, 4, 5] focused on the estimation of ToA with the use of a low-complexity algorithm. However, the low-complexity algorithm could not determine the DP that passed through an obstacle, and mainly assumed a LOS environment. Correspondingly, [6, 7] did not take into account the effects of the obstacles because the primary goal of these studies was to overcome the sampling rate limit of the system. [8, 9, 10] suggested algorithms that estimate ToA even under severe conditions, but the algorithm focused only on low- signal-to-noise ratio (SNR) cases. Low-DP power level cases were not the primary considerations of these studies. [11, 12, 13, 14] considered the interference caused by the multipath which affected the DP estimation, but the DP attenuation owing to the obstacle was assumed to be small. This was unrealistic because obstacles in a typical indoor environment, e.g., walls, desks, and partitions, generate transmission losses in the range of 10 to 20 dB at operating frequencies in the range of 2 to 5 GHz. These papers were only concerned about the performance based on the SNR of the entire signal.

To prevent false detection, research to find the DP in environments where obstacles exist has been performed [15, 16]. However, the proposed method showed that if the DP passes through obstacles causing high attenuation, it is not easy to detect the DP. Yang *et al.* [17, 18] focused on the fact that a longer preamble signal consisting of a pseudo noise (PN) sequence used in the communication system yields clearer observation of the path in the correlation function (CF) between the received signal and the preamble signal. [17, 18] proposed measuring the ToA of the path more accurately by connecting the demodulated data to the end of the preamble signal which generates the same effect as using a longer preamble signal. However, this result is achieved by using data demodulation applying the least-squares (LS) estimator in systems with low order quadrature amplitude modulation (QAM). If the QAM order increases, the effect of increasing noise is more significant than the effect that the path becomes clear in the CF when the demodulated data is placed at the end of the preamble because of errors that arise in the demodulated data. This method is not suitable for broadband communication systems such as 802.11ac, because the increased noise makes the path difficult to distinguish. Chetty *et al.* [19] proposed a method that iteratively finds the highest value in the CF and subtracts a small gain of this time index until the highest value is lower than a threshold instead of data demodulation to distinguish the DP from multiple paths. However, it is not suitable for general indoor communication systems, as it requires a very high SNR.

In this chapter, I propose a new method that can be used with high order QAM and an appropriate SNR. I introduce two independent novel estimators and propose a method for detecting the low power DP by combining the advantages of both estimators. One estimator uses enhanced interference cancellation, which estimates and repetitively removes the interference generated from undesired strong paths around the DP via a super-resolution technique. The other is a novel path detector that improves the detection performance by combining the CF and the estimated channel to observe each path more clearly. I propose performing DP detection through the intersection of results obtained independently from the two estimators. The proposed method is not affected by the QAM order, because the demodulated data is not used in the algorithm, and it is designed to operate at the SNR of a general communication environment by combining the result of the interference elimination with the new estimator. The performance evaluation of the combination of the two methods in various environments using the 802.11ac system shows that the proposed method has better performance than the existing methods.

The remainder of this chapter is organized as follows: Section 4.2 describes the system model and defines the problem. Section 4.3 explains the proposed interference cancellation technique and the enhanced path detection method. Additionally, after explaining the reason why the two algorithms should be combined, I describe a method for combining the two suggested algorithms. Various environments for performance evaluation and the corresponding DP estimation results are provided in Section 4.4. Moreover, the distribution of the DP estimation error is modeled so that the ranging performance can be applied to localization algorithms. Section 4.5 outlines the conclusions.

## 2.2 System Model and Problem Definition

In this study, ToA estimation is considered in orthogonal frequency-division multiplexing (OFDM) systems used in various communication systems such as Wi-Fi and long term evolution(LTE). A typical OFDM system performs ToA estimation and time synchronization using a PN-based preamble signal which has a sharp autocorrelation function. Considering an OFDM system with $N$ subcarriers, the transmitted preamble in the discrete time domain $x[n]$ can be written as

$$x[n] = \sum_{k=0}^{N-1} X_k e^{\frac{j2\pi kn}{N}}, \tag{2.1}$$

where $X_k$ represents the preamble data transmitted over the $k$th subcarrier. $x[n]$ is passed through a digital-to-analog converter (DAC) and a multipath channel $h(t)$. The multipath channel can be represented by the sum of several delta functions, as follows:

$$h(t) = \sum_{u=0}^{N_p-1} a_u \delta(t - \tau_u), \tag{2.2}$$

where $a_u$ and $\tau_u$ are the complex channel gain and ToA of each path, respectively, and $N_p$ is the total number of paths. The received signal converted to the baseband after passing through the multipath channel is

$$y(t) = x(t) * h(t) + w(t), \tag{2.3}$$

where $x(t)$ is the transmitted baseband signal after passing through the DAC, $w(t)$ is the zero-mean complex additive white Gaussian noise, and $*$ represents convolution. The received signal $y(t)$ is converted into a discrete time domain signal $y[n]$ by an analog-to-digital converter. Typical OFDM systems, such as Wi-Fi, LTE, and Wibro, obtain the ToAs of each path by finding the peaks in the square of the cross-correlation function $C$ between the received signal and transmitted preamble signals, where

$$C[m] = \sum_{n=0}^{N-1} \overline{x[n]} y[m+n]. \tag{2.4}$$

Here, $\overline{(\cdot)}$ represents the complex conjugate, and $m$ is the time index of $C$.

When an obstacle interferes with the multipath, including the direct path, the modified multipath channel $h'(t)$ is expressed as follows:

$$h'(t) = \sum_{u \in O} \frac{a_u}{\zeta_u} \delta(t - \tau_u) + \sum_{u \notin O} a_u \delta(t - \tau_u), \tag{2.5}$$

where $O$ is the set of indices of the path that penetrates the obstacle, and $\zeta_u$ is the transmission loss. The goal of this study is to find $\tau_0$ using the transmitted, received, and preamble signals when $10log_{10}(\zeta_u^2)$ is significantly high (approximately in the range of 10-20 dB).

Detection of DP which passes through an obstacle is difficult for two reasons. First, there is interference from the adjacent nonsample-spaced paths [20]. As described in [20] and [21], if the delay of the path is not an integer multiple of the sampling time $T_s$, the energy of the path leaks into the adjacent sample-spaced taps. Interference from adjacent nonsample interval paths causes an error owing to the leakage of the adjacent strong path that is being incorrectly estimated as the shortest path instead of as the low-power DP. Therefore, to detect the DP more accurately, it is necessary to remove the interference from the adjacent paths. Fig. 2.1 shows an example of when it is difficult to detect the DP. Fig. 2.1 (a) describes the illustration of the interference from adjacent paths. The interference generated from the adjacent paths is leaked and adversely affects the detection performance of the DP.

The second reason is that owing to the low power of the DP, $|C|^2$ does not have a sufficiently high value at the ToA of the DP, even if the autocorrelation of the PN sequence exhibits sharp peaks. Even without any interference, the increased attenuation owing to the obstacle makes it difficult to distinguish the DP from noise. It is difficult to detect a low-power DP using a simple thresholding technique alone. Examples of a situation where the presence of an obstacle makes the DP detection difficult are shown in Fig. 2.1 (b). LOS is blocked by an obstacle, and the DP in the CF does not exceed the threshold. No low-power DP are detected, and a high-power path arriving at a subsequent time is mistaken as the DP. An arbitrary lowering of the threshold to solve this problem may cause performance deterioration because it causes noise with high power as well as the paths to exceed the threshold.

## 2.3 Proposed Method

In this section, for solving the two problems mentioned above, two independent methods are proposed to enhance the accuracy of DP detection in OFDM-based positioning systems. Since the tasks of removing the interference and distinguishing the DP from the noise are independent of each other, the two methods are performed separately, and subsequently their results are combined to improve the detection performance for finding the DP.

### 2.3.1 Successive Path Detection with Interference Cancellation

In this subsection, I propose an algorithm to detect and remove paths with high power from the received signal step-by-step to remove interference from the path adjacent to the DP. This algorithm is used to prevent paths other than the DP from being determined as shortest paths. The proposed successive path-detection algorithm with interference cancellation starts by estimating the ToA of the strong paths in subsample units to measure the interference from the paths. To estimate the ToA of the subsam-

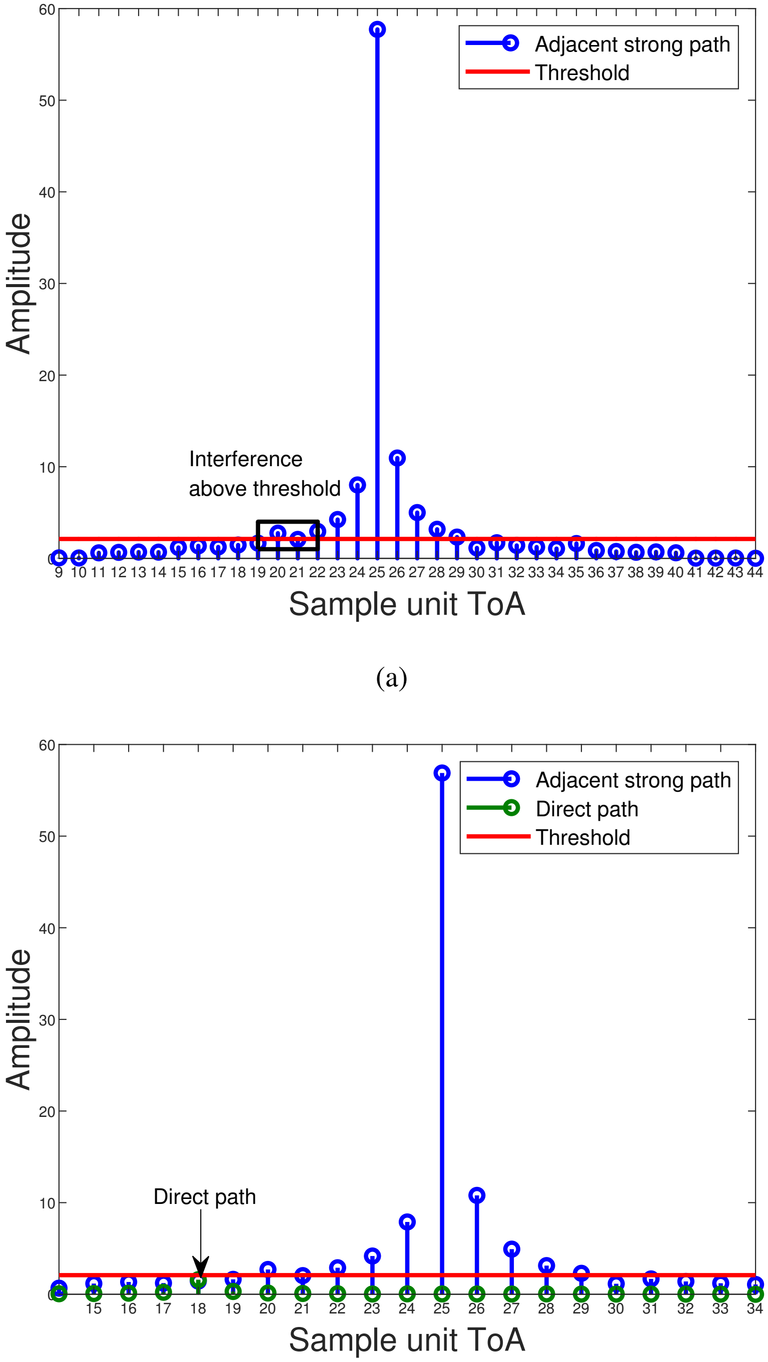

(a)

(b)

Figure 2.1: An example of when it is difficult to detect the DP. (a) The interference generated from the adjacent paths, (b) Low-power DP

ple unit, the proposed algorithm employs a super-resolution technique with a modified maximum peak-to-leaking ratio (MPLR) algorithm [15], which has a relatively low computational complexity and high performance. The detailed procedure is as follows:

The estimated ToA in the MPLR is summarized as

$$\{\hat{\theta}, \hat{\epsilon}\} = \arg\max_{\hat{\theta},\hat{\epsilon}} \frac{\left|\hat{h}_{\hat{\theta}}(\hat{\epsilon})\right|^4}{\frac{1}{\hat{\theta}}\sum_{n=0}^{\hat{\theta}-1}\left|\hat{h}_n(\hat{\epsilon})\right|^2}, \tag{2.6}$$

where $\hat{\theta}$ and $\hat{\epsilon}$ are the estimated ToAs in the sample unit and sub sample unit, respectively, and $\hat{h}_n(\hat{\epsilon})$ is the estimated time shifted channel, which is obtained as follows:

$$\hat{h}_n(\hat{\epsilon}) = \frac{1}{N}\sum_{k=0}^{N-1} X_k{}^{-1}\widetilde{y}_k^r e^{j\frac{2\pi k\hat{\epsilon}}{N}\frac{2\pi kn}{N}}, \tag{2.7}$$

where $\widetilde{y}_k^r$ is the value corresponding to the $k$th frequency of the $N$-point discrete Fourier transform on $\{y[r], y[r+1], ...$ $, y[r+N-1]\}$, which refers to the received time-domain signal extracted from the time sample $r$. $r$ is defined as the time sample in which $|C|^2$ exceeds the threshold $T$ for the first time, and $T$ is set to the value obtained from the white Gaussian noise characteristic as proposed in [22]:

$$T = \sqrt{-\ln(P_{FD}/L)2\hat{\sigma}_F^2}, \tag{2.8}$$

where $P_{FD}$ is the probability of false detection, $L$ is the length of the cyclic prefix, and $\hat{\sigma}_F^2$ is the estimated noise variance.

In this study, to reduce the amount of computation, $\hat{\theta}$ is set to the time index of the maximum peak ($\theta_M$) which is obtained from $|C|^2$. The proposed algorithm estimates $\hat{\sigma}_F$ as

$$\hat{\sigma}_F = \sqrt{\frac{2}{\pi}}\left(\max\{|C|^2\}\right), \tag{2.9}$$

instead of using the average value of $|C|^2$ as applied in [22].

Once the ToA of the strong paths is measured through the aforementioned procedure, the interferences from these paths are estimated and removed from the received signal. The form of the interference is assumed to contain a time shifted sinc function as in [20], but it changes when a specific filter is applied to the transceiver. Considering the filter applied in the transceiver, if the form of the interference is defined as $f_{tr}(t)$, the sample interval interference due to the delay $t_p$ is given by

$$\hat{f}_l[n] = \begin{cases} \delta[n - \frac{t_p}{T_s}], & \text{if } t_p = \text{integer multiple of } T_s \\ f_{tr}(nT_s - t_p), & \text{otherwise .} \end{cases} \tag{2.10}$$

The amplitude of $\hat{f}_l[n]$ is adjusted as follows:

$$\hat{f}_{l_2}[n] = \hat{f}_l[n] \cdot \frac{\hat{h}_{\theta_M}(0)}{\max f_l[n]}, \tag{2.11}$$

so that the maximum value is equal to $\hat{h}_{\theta_M}(0)$. After the estimated interference is modified, it is convolved with the transmitted signal, and then removed from the received signal, as follows:

$$y_1[n] = y[n] - \hat{f}_{l_2}[n] * x[n], \tag{2.12}$$

where $y_1[n]$ is the resultant signal after the interference elimination process.

Finally, the proposed algorithm iteratively performs the strong path detection and interference elimination until no strong path remains. In the $i$th iteration, the signal after the interference prediction and elimination is expressed as

$$y_i[n] = y_{i-1}[n] - \hat{f}_{l_2}[n] * x[n], \tag{2.13}$$

where $y_i[n]$ is the signal after the interference elimination in the $i$th iteration. In every iteration, the ToA of the earliest path that exceeds the threshold is stored in the set $F_A$ and compared with the results of the algorithm presented in 2.3.2.

### 2.3.2 Enhanced Path Detection Using CFAR

This subsection presents another algorithm that is independent of the method presented in 2.3.1. The enhanced path detector reduces the non-detection rate due to the low power of the DP in a manner independent of interference cancellation. Since it is not easy to make the DP more clearly observable at $C$ by increasing the power of the DP or the gain of the PN sequence once the communication system is already determined, I solved the problem by suggesting a new estimator.

I proposed the use of the product of $C$ and estimated channel $\hat{h}^d[n] = \hat{h}_n(0)$ as a new function to observe the DP more clearly and enhance the path detection performance. $C$ and $\hat{h}^d$ differ from each other in their calculation method and purpose, but each exhibits a peak at the ToA of the path and a low value (noise) at other times; thus, if the two are combined, the path can be observed more clearly than by using $C$ alone for DP detection. Since both functions are similar to the multipath channel $h[n]$, combining $C$ and $\hat{h}^d$ can be likened to squaring $C$. However, one difference is that when combining these two functions, the increase of the noise is smaller than the increase of the value corresponding to the path. Thus, the peak height is increased at the ToA of the path, which exhibits the effect of increasing the SNR of the path when $C$ and $\hat{h}^d$ are multiplied. Since a high SNR improves the performance of the peak detection algorithm using the constant false alarm rate (CFAR) method [23], the DP detection performance can be improved by combining $\hat{h}^d$ and $C$. This can be mathematically represented as follows:

According to [17], the value of $C$ at DP's ToA $m_0$ is expressed as

$$\begin{aligned} C[m_0] = Nh[m_0] &+ \sum_{u=1}^{N_p-1} D[m_0 - m_u]h[m_u] \\ &+ \sum_{n=0}^{N-1} w[m_0+n]\overline{x[n]}, \end{aligned} \tag{2.14}$$

where $m_u$ is the ToA of the $u$th path, $h[m_u]$ is the channel in the discrete time domain, and $D[m_0 - m_u]$ is the correlation between $x[n]$ and $x[n + m_0 - m_u]$. The estimated channel using the LS method contains noise, is as follows:

$$\hat{h}^d[m_u] = h[m_u] + g, \tag{2.15}$$

where $g$ is the error generated while estimating the channel $h[m_u]$. If $P$ is defined as the product of $C$ and $\hat{h}^d$,

$$P[m] = \left| C[m] \cdot \hat{h}^d[m] \right|, \tag{2.16}$$

the ratio of $P$ at $m_0$ to $P$ at $m_1$ is

$$\begin{aligned} &\frac{P[m_0]}{P[m_1]} = \\ &\left| \frac{N\left\{h[m_0]\right\}^2 + h[m_0] \sum\limits_{u=1}^{N_p-1} D[m_0 - m_u]h[m_u] + g_2}{h[m_1] \sum\limits_{u=0}^{N_p-1} D[m_1 - m_u]h[m_u] + {g_2}'} \right|, \end{aligned} \tag{2.17}$$

where $m_1$ is the nearest time index with $m_0$. In a typical communication environment, this ratio is approximated as

$$\begin{aligned} &\left| \frac{Nh[m_0] + \sum\limits_{u=1}^{N_p-1} D[m_0 - m_u]h[m_u] + \frac{g_2}{h[m_0]}}{\frac{h[m_1]}{h[m_0]} \left( \sum\limits_{u=0}^{N_p-1} D[m_1 - m_u]h[m_u] + \frac{{g_2}'}{h[m_1]} \right)} \right| \\ &\approx \left| \frac{h[m_0]}{h[m_1]} \cdot \frac{C[m_0]}{C[m_1]} \right|. \end{aligned} \tag{2.18}$$

If the function $|h|$ has a peak at $m_0$, $|h[m_0]/h[m_1]|$ has a value greater than one. Therefore, $P$ has a relatively high peak at $m_0$ compared with $C$, and the probability of successful detection via the peak detection algorithm increases. This certainly indicates that $P$ is useful for DP detection.

In addition, I can further enhance the DP detection performance by applying the log function to $P$. The reason for using the log function is that the performance of the peak detector is affected by the coefficient of variation (CV) [24], which is defined as the ratio of the signal's standard deviation to the mean. In general, the peak detection process performs well when CV is in the range of 0.1 to 5 [24]. Thus, $P$ values (CV $=$ 19.631) are transformed through the log function to decrease the CV value. When the log function is applied, the CV attains a value of 0.112, which is

Table 2.1: K–S Statistics Between Several Distributions and Enhanced Path Detector

| **Distribution** | **K–S Statistics** | **p value** |
|---|---|---|
| Weibull | 0.0287 | 0.46 |
| Lognormal | 0.0659 | 0.0017 |
| Normal | 0.0661 | 8.2E-4 |
| Uniform | 0.0691 | 1.9E-5 |
| Gamma | 0.0735 | 6.8E-6 |
| Rayleigh | 0.2650 | 0 |

appropriate for applying the peak detector. Therefore, in this chapter, I propose using $E = [\log_{10}(P) - \{\min \log_{10}(P)\}]$ for DP detection. The minimum value of the log function was subtracted to keep the function positive.

The DP is detected by applying the CFAR algorithm at the obtained $E[n]$. As $\hat{h}^d$ has a Gaussian distribution and $C$ has Rayleigh distributions, the distribution of $E$ is not expressed by a simple distribution function such as the gamma distribution. Instead, Kolmogorov–Smirnov (K–S) tests with a large number of experimental results reveal that $E$ closely follows the Weibull distribution. Table 2.1 compares the results of two-sample K–S tests for several well-known distributions and the empirical distribution of $E$, revealing that the Weibull distribution has the smallest K–S statistics. In the K–S test, the significance level was set to 0.05. The results of comparing the Weibull distribution and distribution of $E$ are shown in Fig. 2.2.

Therefore, in this study, peak detection is performed by applying the CFAR peak detector proposed in [23] with the assumption that the noise has a Weibull distribution, and the result is stored in $F_B$.

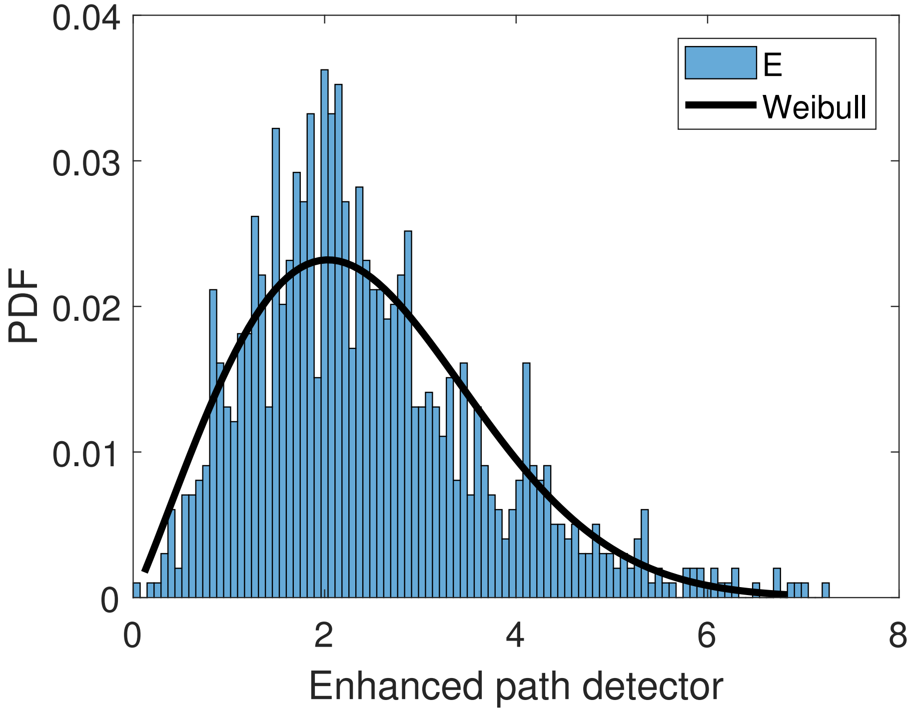

Figure 2.2: Comparison of the probability density function(PDF) of Weibull distribution and a histogram of $E$

### 2.3.3 Combination of Interference Cancellation and Enhanced Path Detector

Once both interference cancellation and the enhanced path detector are used, ToA of the DP is determined by combining these results.

When detecting the DP, false detection is caused by high-power noise and interference from paths with high power. Therefore, the interference cancellation algorithm can reduce the false detection event. However, even though the interference cancellation can remove the influence of adjacent paths, it is not easy to distinguish the DP from noise because the power of the DP does not increase when the interference is removed. Interference cancellation focuses on the reduction of the number of false detection events.

Missed detection is caused when a high-level threshold is applied for path detection. Therefore, it is possible to reduce the number of missed detection events by using an enhanced path detector–an algorithm that raises the power of the DP. However, even though the enhanced DP detector reduces the number of missed detection events by distinguishing the DP from ambient noise, interferences from adjacent paths still exist. Because the problem of interference, noise, and the low power DP is mixed, applying only the interference cancellation algorithm or the enhanced path detector cannot improve the DP detection performance. Therefore, in this study, an improved DP detection performance was obtained based on the combination of the interference cancellation technique and the enhanced path detector. The ToA of the DP is estimated by taking the intersection of the obtained results and choosing the earliest one among them.

$$F_C = \min(F_A \cap F_B). \tag{2.19}$$

A block diagram of the entire process is shown in Fig. 2.3.

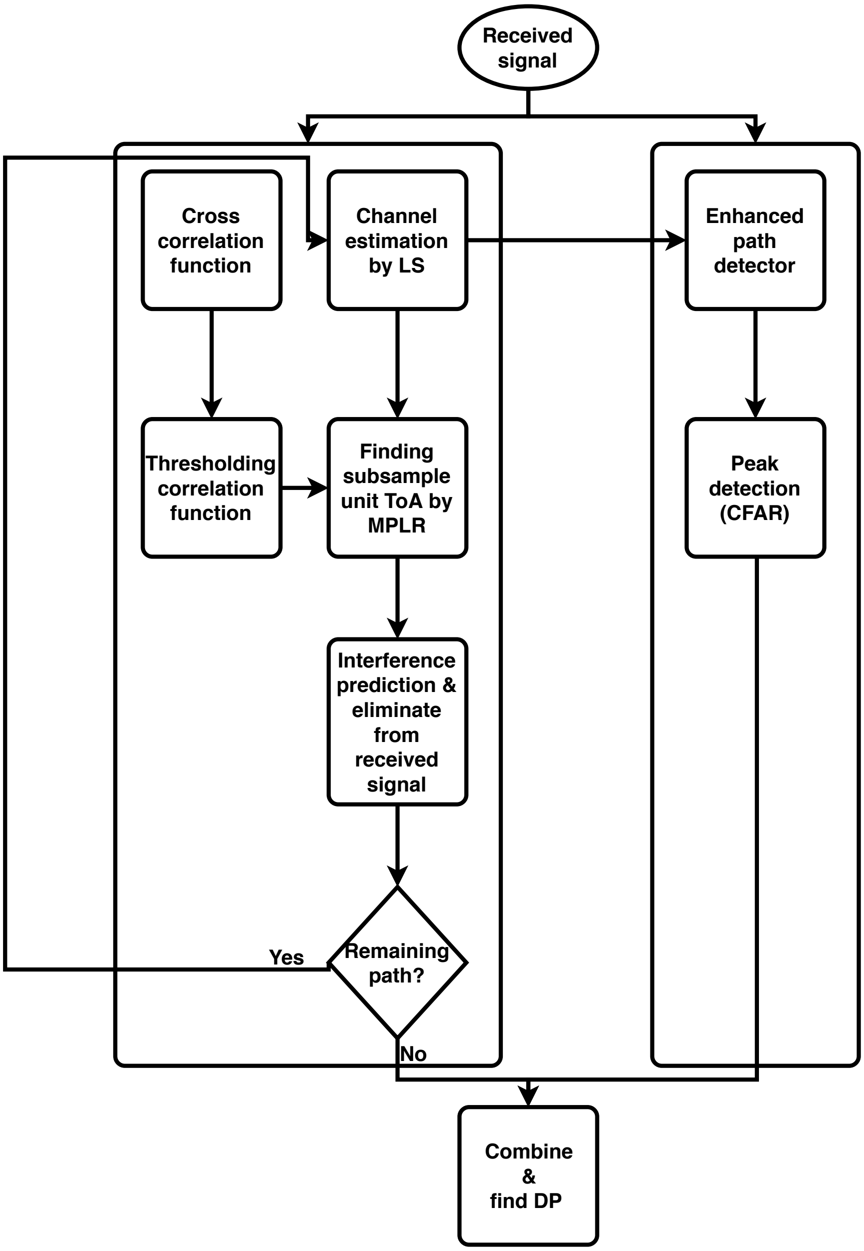

Figure 2.3: A block diagram of the entire process

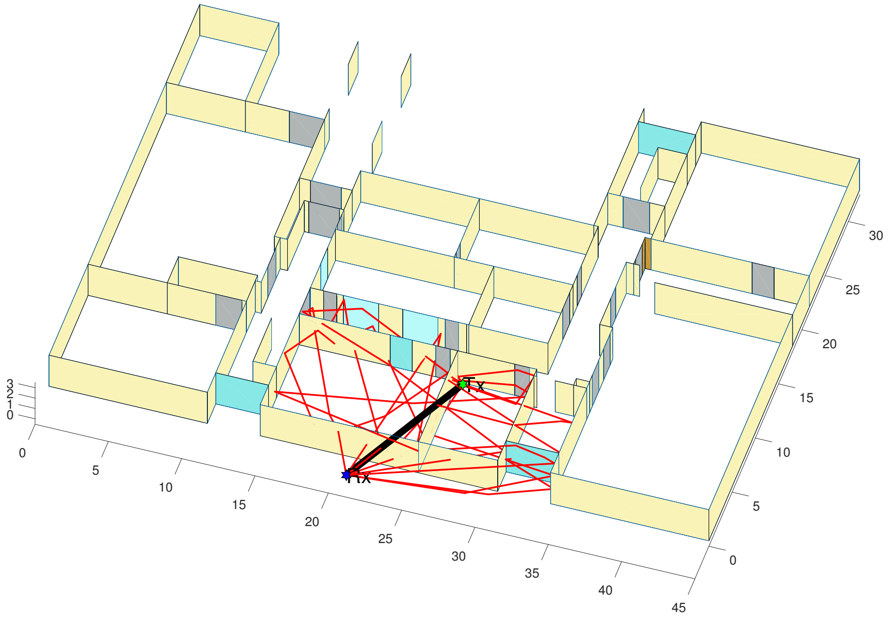

(a)

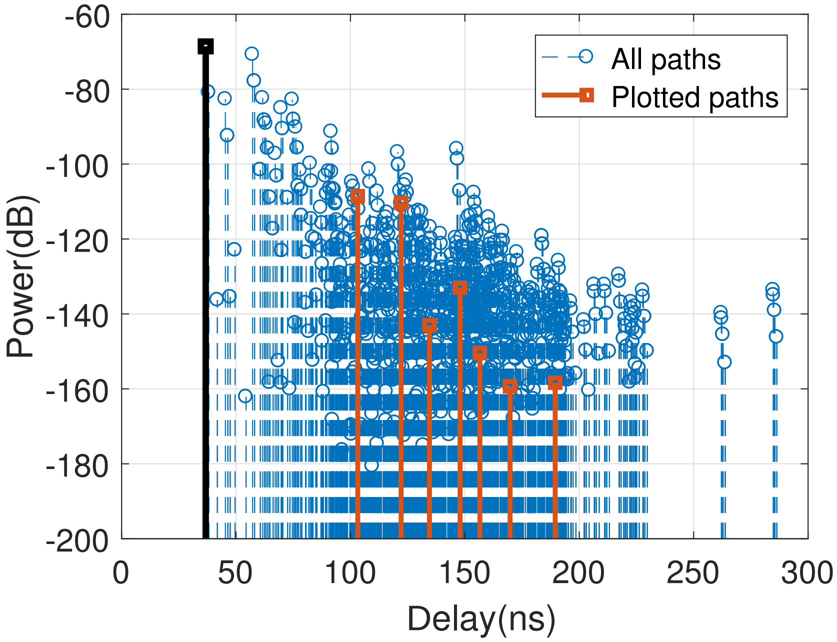

(b)

Figure 2.4: An example of ray tracing result (a) Some of the rays traced in an academic building, (b) Time domain channel impulse response.

## 2.4 Numerical Results

To evaluate the performance in a wide range of environments, I tested the performance in channel environments obtained with a three-dimensional ray-tracing tool [25, 26]. The ray tracing results for a specific environment are shown in Fig. 2.4. Fig. 2.4 (a) describes some of the rays traced in an academic building (INMC). The material of each wall is shown in color, and the line marked in black indicates the DP. Fig. 2.4 (b) describes the time domain channel impulse response. As plenty of rays exist, only some of the rays are plotted in Fig. 2.4 (a), and the black line indicates the DP. The receiver was installed at intervals of 1 m, and the performance at each point was evaluated. Since the indoor environment has different shapes depending on the usage, there is a difference in the channel environment, which causes a difference in the ranging performance. Therefore, in this study, various types of buildings were chosen as performance evaluation sites to consider various situations. The experimental environments were selected as an academic building (INMC, ASRI on the Seoul National University campus), a general office space (office at the Electronics and Telecommunications Research Institute, ETRI), and general residential space (APT). The shape of each environment is shown in Fig. 2.5. In this study, the power of the DP was reduced by 20 dB to simulate the presence of obstacles in the path between the transceivers. The Wi-Fi system (802.11ac), which is widely used in indoor environments, is applied as the communication system, and an overview of the system used in the experiment is shown in Table 4.1.

Fig. 2.6 shows the cumulative distribution functions (CDFs) for the absolute value of the measurement error obtained from the Monte Carlo trial in various environments. The proposed DP detection algorithm shows lower error than conventional algorithms in all environments. Notably, the proposed method has shown remarkable performance in all cases, even though the experiment was performed not only when the power of the DP is low but also when the DP is the strongest path. This result differs from the conventional methods that show improved performance only when the DP is the

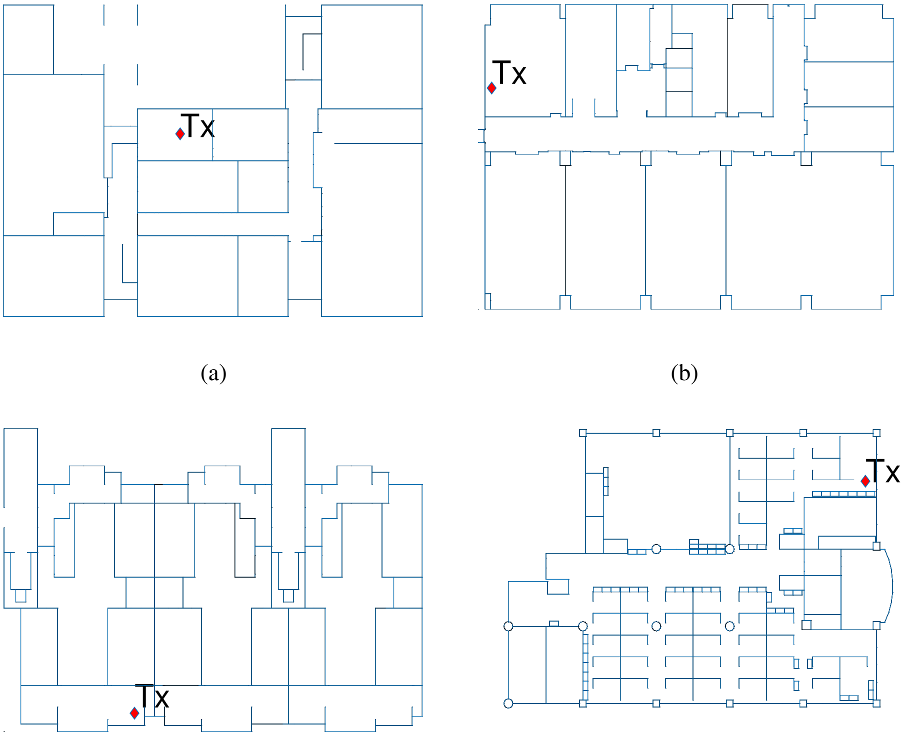

(a) (b)

(c) (d)

Figure 2.5: The floor plans for various environments (a) INMC (academic building), (b) ASRI (academic building), (c) APT (general residential space), (d) ETRI (general office space)

Table 2.2: System Parameters

| **Symbol** | **Parameters** | **Values** |
|---|---|---|
| $f_C$ | Center frequency | 5 GHz |
| $P_t$ | Transmit power | 20 dBm |
| $N_0$ | Noise floor | -90 dBm |
| $N$ | FFT Length | 256 |
| $f_S$ | Sampling rate | 160 MHz |
| $L$ | Cyclic prefix length | 64 |
| $Q$ | QAM order | 64 |
| $\delta\epsilon$ | Interval between $\hat{\epsilon}$ | 0.01 |
| $P_{FD}$ | False detection rate | $10^{-9}$ |

strongest or has low power. The distribution of the errors in each building shows that the performance of the algorithm changes drastically as the environment changes. In the case of ETRI, i.e., which is a typical office space with a partition for each personal space, the proposed algorithm has excellent performance compared with conventional methods, as the partitions serve as obstacles between the transceivers. Since the proposed method is designed for an environment in which obstacles exist, a larger number of obstacles increases the performance difference between the conventional methods and the proposed algorithm. However, in the case of the APT environment, the performance improvement of the proposed algorithm was smaller than that for the ETRI environment because there were only a few reflective objects, such as the iron door. Since an environment with few reflective objects produces a channel with the DP having the highest power among the paths, ranging requires only finding the ToA of the path with the highest power among all paths. Thus, the proposed method does not show a significant performance improvement in this environment. Meanwhile, the performance in the ASRI and INMC environments showed a similar pattern, but the

INMC environment yielded a slightly higher performance than the ASRI one owing to the existence of iron structures such as iron doors and elevator doors. Table 3.2 compares the root-mean-square errors (RMSEs) for the application of the proposed method in various environments. In the ETRI and INMC environments, the proposed algorithm has a lower RMSE than in other environments, and it can be observed that the accuracy of ranging increases significantly when the proposed method is used, in all four environments.

Additionally, Fig. 2.6 shows that the proposed algorithm elicits a significantly better performance than conventional methods. The reason why conventional algorithms elicit a reduced performance in the test environment is as follows.

First, in an environment where obstacles exist, the DP was not detected by identifying the path with the greatest power as presented in [27] because the power of DP is not the maximum between multipaths.

Secondly, the threshold-based DP detection scheme presented in [22] elicited a poor performance in both the LOS/NLOS environments because it did not remove the interference generated in the path with high power. Thirdly, the interference cancellation-based algorithm presented in [17, 18] assumed a four-QAM system and used least-squares demodulation to recover data and generate an enhanced path detector. In systems that use high QAM, such as 802.11ac, the least-squares demodulation technique generates considerably larger error rates. The path detector that used recovered data yielded increased error rates, that led to significant performance degradation in the test environment.

Conversely, the algorithm presented in this study yielded excellent performance in both the LOS and NLOS environments. Instead of using the recovered data, the appropriate interference cancellation method was used which employed the super-resolution method. Furthermore, the proper distinction between noise and the path achieved by an enhanced path detector led to a performance difference compared to conventional techniques.

Table 2.3: RMSE of the estimated range

| | INMC | ASRI | APT | ETRI |
|---|---|---|---|---|
| Threshold [22] | 4.95 m | 6.09 m | 6.97 m | 5.00 m |
| Maximum [27] | 4.60 m | 5.46 m | 5.07 m | 3.77 m |
| IC [17] | 8.53 m | 8.82 m | 9.48 m | 9.21 m |
| Proposed | 2.75 m | 3.06 m | 4.19 m | 2.11 m |

To show the improvement in performance when various environments are combined, in Fig. 2.7, I plot the CDF by combining the performance for all the environments. It can be seen that the proposed algorithm shows improved performance, even in various environments. The median of the absolute error of the proposed algorithm is 0.85 m, which is significantly small compared with the conventional algorithm which shows a median value of 2 to 5 m. The high-performance results verify that combining the enhanced path detector and the interference cancellation is feasible in indoor environments.

If the ranging result obtained using the proposed algorithm is applied to the positioning algorithm, such as [28], it is expected to have an error of approximately 1 m. The results show that the proposed algorithm, which does not require calibration, has significance for positioning, considering that the accuracy of the current indoor positioning algorithm using fingerprinting is 1.2 m, as described in [29].

Combining the interference cancellation and the enhanced path detector increases the computational load compared to when the algorithms are executed by themselves. However, the combined algorithm improves the ranging performance significantly by making the DP detectable even in a non-line-of-sight (NLOS) environment. Therefore, to assure reliable performance in various environments, it is reasonable to combine the interference cancellation with the enhanced path detector.

I also modeled the distribution of the error by fitting it to various distributions for the ranging error model to be used in positioning algorithms. The error was used as

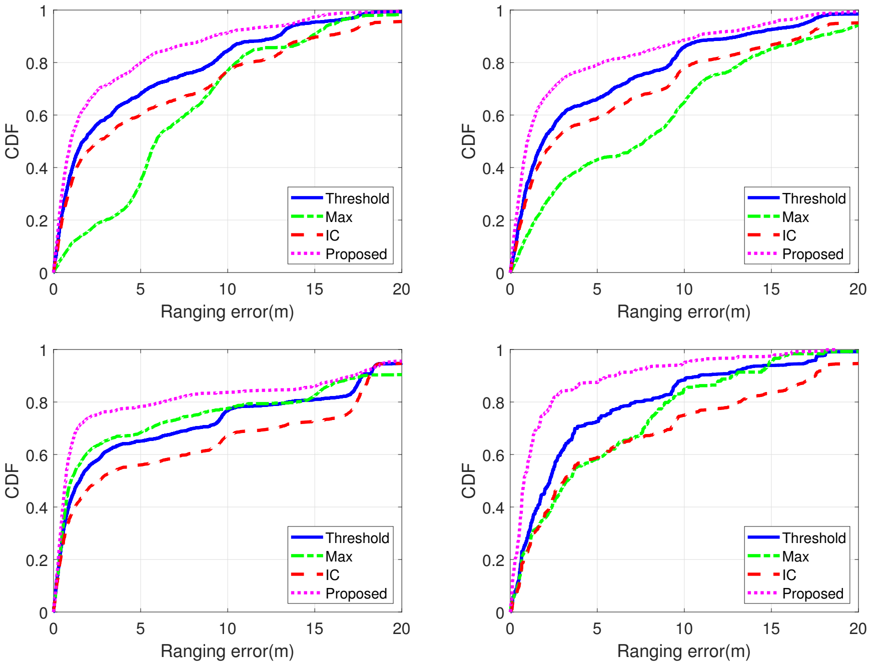

Figure 2.6: Empirical CDF in various environments with proposed (pink), thresholding [22] (blue), interference cancellation [17] (red), finding maximum path [27] (green) algorithm (a) INMC (academic building), (b) ASRI (academic building), (c) APT (general residential space),(d) ETRI (general office space)

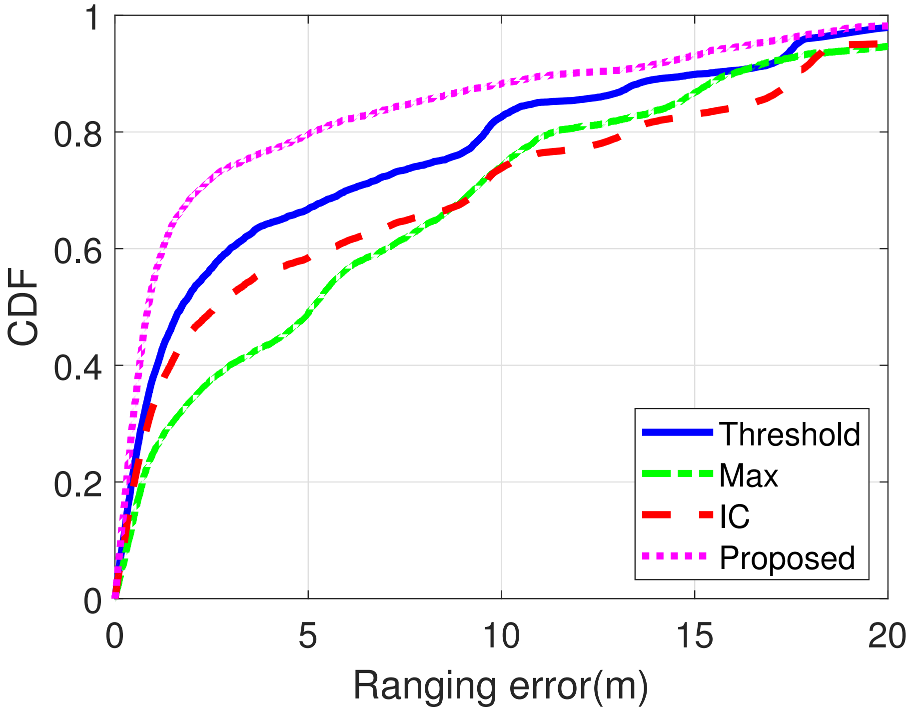

Figure 2.7: Empirical CDF showing comprehensive performance comparison in various environments

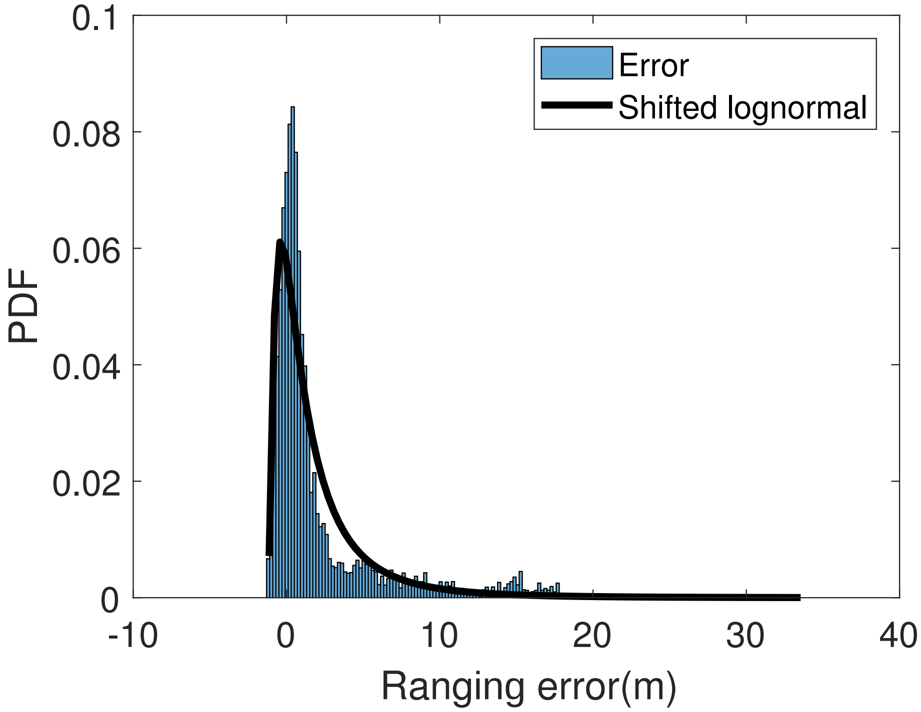

Figure 2.8: The PDF of the error that occurs when using the proposed algorithm.

Table 2.4: K–S Statistics Between Several Distributions and Ranging Error

| **Distribution** | **K–S Statistics** | **p value** |
|---|---|---|
| Weibull | 0.03524 | 0.13 |
| Lognormal | 0.0240 | 0.55 |
| Normal | 0.0428 | 0.046 |
| Gamma | 0.0440 | 0.016 |
| Rayleigh | 0.0503 | 0.012 |

the value obtained by subtracting the actual range from the estimated range, and the goodness of fitting results obtained using K–S statistics are shown in Table 2.4. In the K–S test, significance level was set to 0.05. The analysis reveals that the shifted lognormal with the distribution of

$$f(x;\mu,\sigma,\eta) = \frac{1}{(x-\eta)\sigma\sqrt{2\pi}} e^{\left\{-\frac{[\ln(x-\eta)-\mu]^2}{2\sigma^2}\right\}}, \tag{2.20}$$

where $\mu$, $\sigma$, and $\eta$ are the parameters of the distribution, is most similar to the error distribution.

The parameters of the shifted lognormal distribution are estimated by the maximum likelihood estimation method which maximizes the log likelihood. The log likelihood is defined as follows:

$$lnL(X:\mu,\sigma,\eta) = \sum_{\beta=1}^{\alpha} ln[\frac{1}{(x-\eta)\sqrt{2\pi}\sigma} e^{\frac{-(ln(x-\eta)-\mu)^2}{2\sigma^2}}], \tag{2.21}$$

where $X = (x_1, x_2, x_3, ...x_\alpha)$ is the set of random observations from the PDF of ranging error, and $L(X:\mu,\sigma,\eta)$ is the likelihood function. By differentiating equation

(2.21), three equations are obtained for parameter estimation, as follows,

$$
\begin{aligned}
\frac{\partial ln(X:\mu,\sigma,\eta)}{\partial\mu} &= \sum_{\beta=1}^{\alpha}[\frac{ln(x_\beta-\eta)-\mu}{\sigma^2}]=0\\
\frac{\partial ln(X:\mu,\sigma,\eta)}{\partial\sigma} &= \sum_{\beta=1}^{\alpha}[-\frac{1}{\sigma}+\frac{(ln(x_\beta-\eta)-\mu)^2}{\sigma^3}]=0\\
\frac{\partial ln(X:\mu,\sigma,\eta)}{\partial\eta} &= \sum_{\beta=1}^{\alpha}[-\frac{1}{x_i-\eta}+\frac{(ln(x_\beta-\eta)-\mu)^2}{\sigma^2(x_\beta-\eta)}]=0.
\end{aligned}
\tag{2.22}
$$

Unlike the unshifted lognormal distribution, parameter estimation for a shifted lognormal distribution is a problem that requires the solution of a nonlinear function [30]. Therefore, this study used the iterative quasi-Newton method which is presented in [30]. The quasi-Newton method solves the problem using an iterative procedure as follows,

$$
\begin{aligned}
&\text{(1) Set initial value of } \mu_\lambda,\sigma_\lambda,\eta_\lambda\\
&\text{(2) Find } p_\lambda=-H_\lambda g(\mu_\lambda,\sigma_\lambda,\eta_\lambda)\\
&\text{(3) Evaluate } (\mu_{\lambda+1},\sigma_{\lambda+1},\eta_{\lambda+1})=(\mu_\lambda,\sigma_\lambda,\eta_\lambda)+\gamma p_\lambda,
\end{aligned}
\tag{2.23}
$$

where $\lambda$ is the iteration step, $\mu_\lambda,\sigma_\lambda,\eta_\lambda$ are the estimated parameters at the $\lambda$th step, $p_\lambda$ is a 3×1 vector of the search correction factors, $H_\lambda$ is a 3×3 matrix of the second partial derivatives, $g(\mu_\lambda,\sigma_\lambda,\eta_\lambda)$ is a 3×1 vector of the gradients evaluated at $(\mu_\lambda,\sigma_\lambda,\eta_\lambda)$, and $\gamma$ is the step size. The iteration is repeated until $|(\mu_\lambda,\sigma_\lambda,\eta_\lambda)-(\mu_{\lambda+1},\sigma_{\lambda+1},\eta_{\lambda+1})| < \chi$ where $\chi$ is the tolerance value. When I set $\chi=10^{-2}$, the estimated parameters values obtained using the maximum likelihood estimator were $\mu$ = 1.44, $\sigma$ = 1.73, and $\eta$ = 1.26.

The error distribution was observed to be biased in the positive direction. This is because when the DP is greatly attenuated by an obstacle, the path that arrives after the DP is incorrectly estimated as the shortest path. Since this case is more common than the case where the power of the noise that occurs before the ToA of the DP is especially strong and estimated as the shortest path, the distribution of error follows a lognormal distribution, which has a tail towards the positive direction. Therefore, I suggest assuming that the distance error has a lognormal distribution when using the proposed algorithm in positioning. A comparison of the error distribution with the lognormal distribution is shown in Fig. 2.8.

## 2.5 Summary

In this work, I developed an efficient and robust DP detection scheme for indoor positioning based on wireless communication systems. The motivation was to perform accurate ranging even in an environment where obstacles block the line-of-sight. The proposed method was developed on the basis of interference cancellation and an enhanced path detector. By subtracting the interference from the received signal, low power DP was distinguished from adjacent paths. An enhanced path detector was proposed independently of the interference cancellation method, and the results of both methods were employed together to detect the DP. The simulation results show that the ranging performance of the proposed algorithm tested in various environments is superior to the conventional methods. When there are many obstacles, the performance difference compared with the existing method is particularly large. I also investigated the distribution of the error by fitting it to various distributions. The fitting results obtained through the K–S test show that the distribution of errors is similar to a lognormal distribution. By using the proposed algorithm and error distribution model for ranging, it is expected that the positioning performance will be greatly improved.

# Chapter 3

# Improving the Accuracy of Millimeter Wave Ray Tracing Simulations by Modeling Roadside Trees

## 3.1 Motivation

In order to meet increasing data traffic demands, the millimeter wave frequency band became a candidate spectrum for fifth generation (5G) communication systems. As the millimeter wave bandwidth is much broader than that of the ultra high frequency (UHF) band used for conventional communication systems, the allocation of continuous frequency resources is made easier, which can lead to increased capacity for communication systems. However, the millimeter wave channel is strongly influenced by environmental parameters such as obstacles, atmospheric conditions, and rainfall, owing to the inherent feature of millimeter waves[31, 32]. Since millimeter wave frequency band experiences much higher path loss than the UHF band, more accurate channel information is required for network design activities such as base station placement and cell planning.

As characterizing wireless channel based on measurements for numerous areas is cumbersome, channel information is often predicted and analyzed using ray tracing simulation. Because of the greater influence of environmental parameters, the approach to model millimeter wave channels differs from existing techniques used for modeling UHF band channels. These differences are crucial when urban areas are considered, where obstacles such as roadside trees, vehicles, and electric power poles are more prevalent. Thus, it is essential to model these obstacles and to use them in channel prediction.

To analyze the effect of roadside trees on ray tracing simulation, Leonor *et al.* [33] compared the measured results in an anechoic chamber with the results of two-dimensional (2D) ray tracing simulations where appropriate tree models were included. However, since an anechoic chamber represents a specific environment that cannot reflect the entire real world, it is not possible to correctly analyze the effect of roadside trees on outdoor ray tracing simulations using these experimental measurements. Furthermore, 2D ray tracing techniques are inappropriate to depict the three-dimensional (3D) structure of roadside trees accurately. In [34], roadside trees in an urban environment were modeled and included in ray tracing simulations. The results of these simulations were compared with experimental results. However, both results were compared only in limited viewpoints, and no detailed channel analysis was performed. Also, roadside trees were modeled using simple cylindrical shapes, which may cause a lack of flexibility in its application to the real world.

In this chapter, I modeled roadside trees using four distinct methods for more realistic simulation, and I applied these models to ray tracing simulation. I subsequently analyzed the ray tracing simulation accuracy according to the roadside tree modeling method, by comparing the results of simulations with experimental results measured using a channel sounder in multiple locations.

## 3.2 Measurement Setup and Environments

In this chapter, I used experimental data reported in [35, 36] to analyze the differences between the predicted channel using ray tracing simulation, and the measured channel.

### 3.2.1 Measurement System

Field measurements were performed using a wideband millimeter-wave channel sounder developed by Electronics and Telecommunications Research Institute (ETRI) [35]. The channel sounder measured the channel impulse responses by transmitting and receiving a signal with a bandwidth of 500 MHz, and a carrier frequency of 28 GHz. For more precise characterization of a wireless channel, a pseudo-noise code with a length of 4095 bits was transmitted.

An antenna with a $30^\circ$ half-power beam width (HPBW) is installed in the transmitter, and the direction of the antenna is set as shown in Fig. 3.1(a), so that all regions of interest are included. The receiver used two different antennas: an omnidirectional antenna to consider large-scale fading characteristics and a directional antenna to consider small-scale fading characteristics such as the delay spread.

Since the attenuation in the millimeter wave band is significantly larger than the 6 GHz band, it is difficult to measure the small-scale fading characteristic of the channel with an omnidirectional antenna. Therefore, I used a rotating horn antenna for the receiver to capture the multipath components. A horn antenna with a $10^\circ$ HPBW rotated at $10^\circ$ intervals using stepping motors, was used for the receiver.

The transmitter and receiver modules were synchronized using a rubidium oscillator-based timing module. System calibration was performed prior to the experiment, using a direct connection between these modules. The detailed specifications for this system are listed in Table 4.1.

### 3.2.2 Measurement Environments

Channel measurements were performed in Dunsan-dong, Daejeon, Korea, which is an urban environment with many buildings, roadside trees, obstacles, etc. The measurements were performed at 13 points where the line-of-sight was secured. The measurement environment is shown in Fig. 3.1(a). The measurement was performed 50 times using the omnidirectional and directional antennas at each point, where one rotation of the directional antenna in the receiver was counted as one measurement. Moreover, to consider the effect of small-scale spatial fading when measuring the path loss, additional experiments were performed for each receiving point as the omnidirectional antenna was moved 0.5 m and 1 m to the left and right. The measured data from the omnidirectional antenna were averaged at the right and left positions for each receiving point, and the average value was used for numerical analysis. An illustration of the additional experiments is shown in Fig. 3.1(b).

As there were many buildings and roadside trees in the vicinity of the receiver, their inclusion in the ray tracing simulation was required. Measurements were performed during the transition from summer to autumn, when plants were green. I observed a variety of tree species—including ginkgo and platanus—in this location. The average height of the roadside trees was 8 m, the average breast height of the trees was 4.3 m, the average diameter at the breast height was 0.3 m, and the average crown width of the trees was 4 m.

## 3.3 Simulation Methodology

### 3.3.1 Map Generation and Roadside Tree Modeling

A precise 3D model of the measurement environment is required for accurate simulation. I used data from Vworld [37], provided by the national geographic information institute, for constructing the 3D building model of the measurement area. In this chapter, a street map and a satellite map corresponding to the measurement area was manually examined to record the size and position of the roadside trees for more accurate roadside tree information.

I examined four different tree modeling methods. In the first method, roadside trees were modeled as simple pillars, as presented in [34]. The second method modeled trees as if they consisted of two parts: a trunk and a leaf. With the third method, tree crowns were modeled as multiple narrow columns, similar to the model presented

Table 3.1: System Parameters

| **Parameter** | **Value** |
|---|---|
| Center frequency | 28 GHz |
| Channel bandwidth | 500 MHz |
| Maximum Tx power | 29 dBm |
| Transmitter half power beamwidth | 30 ° |
| 10 ° HPBW horn antenna gain | 24.4 dBi |
| 30 ° HPBW horn antenna gain | 15.4 dBi |
| Omnidirectional antenna gain | 5 dBi |
| Multipath delay resolution | 2 ns |

in [33], where point scatterer exists. Finally, in the fourth method, trees were modeled as a combination of the crown, the trunk, and thin pillars. Each modeling method is shown in Fig. 3.2. More complex models represent the actual shape of a roadside tree more accurately.

In this study, I examine how simulation accuracy varies according to each modeling method.

### 3.3.2 Ray Tracing Simulation Method

In this study, I used a 3D ray tracing tool based on the vertical plane launch (VPL) technique to simulate the millimeter wave band wireless channel. The accuracy of the VPL technique presented in [38] was verified by comparing the results of simulations performed at different frequencies with corresponding experimental measurements [39, 40]. In simulating the channel environment, I considered the reflection and diffraction of radio waves in ray tracing simulation. Additionally, I analyzed the ef-

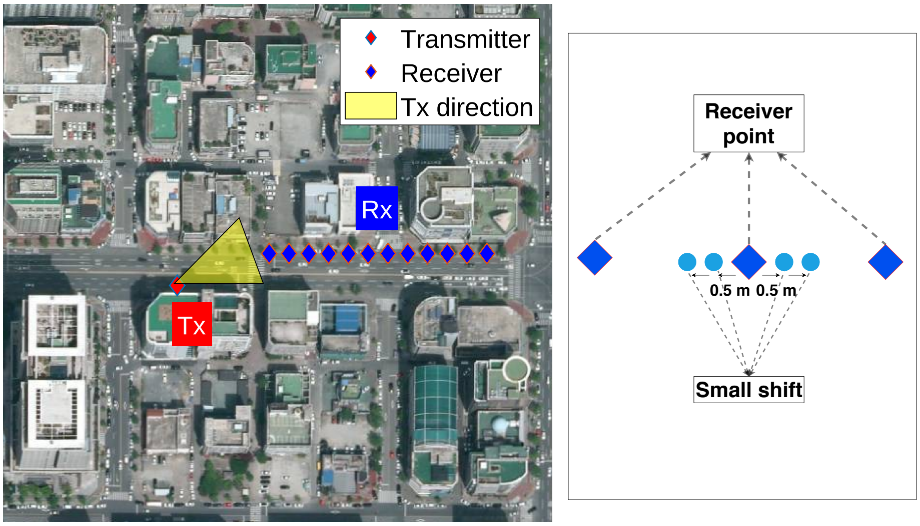

Figure 3.1: Illustration of the measurement environment. (a) Receiver, transmitter. (b) Magnified image of a single receiver location.

fects of the maximum number of reflection and vertical diffraction. The maximum number of reflection varies from 4 to 6, and the maximum number of vertical diffraction varies from 0 to 2. The maximum number of horizontal diffractions was set to 4. Additionally, the material of the building walls consist mostly of brick, concrete, etc, and the relative permittivity of these materials is about 4 to 8 [40]. Thus, the relative permittivity of the buildings in the ray tracing simulation was changed from 4 to 8 to examine how accuracy varies based on this value. In addition, the relative permittivity of tree trunks was set to 9.6, and that of the leaves was set to 10, based on the values given in [41]. The roadside trees were modeled as objects transmitting, reflecting, and diffracting rays. The transmission loss of the roadside tree in the ray tracing simulation was set to 12 dB [43], and the conductivity is assumed to be negligible for the non-conducting buildings. Additionally, for comparison with the experimental data based on the local average for path loss analysis, the ray tracing simulation was performed at the measurement position, and the local average was considered in the simulation.

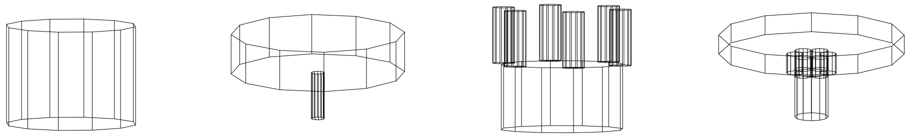

Figure 3.2: Portrayal of various roadside tree modeling methods. (a) Tree modeling using a simple column (b) Separate trunk and leaf modeling. (c) Leaf modeling using a technique similar to the method described (d) Leaf modeling using a variety of structures.

## 3.4 Validation of Ray Tracing Simulation

In this section, I compare the experimental results with the simulation results to investigate how the inclusion of roadside tree models affects the accuracy of ray tracing simulation. I also present a guide for roadside tree modeling based on the analysis of the change in accuracy caused by the selected tree modeling method. For clearer reference, a comparison of the measured data with the simulation result—wherein the maximum number of reflections is set to 6 and the vertical diffraction is set to 1—is shown in Table 3.2.

### 3.4.1 Path Loss Analysis

The root mean squared error (RMSE), mean error, and standard deviation detailed in Table 3.2 was obtained using the difference between the predicted and measured (predicted minus measured) absolute value of path loss. From Table 3.2, it can be seen that the accuracy of path loss prediction improves when roadside trees are modeled, and the RMSE changes according to the tree modeling method. The prediction accuracy of the second method, where tree trunks and leaves are modeled separately, is higher than the accuracy of the first method, where roadside trees are modeled as a simple column. In addition, the path loss predicted when leaves were modeled as a combination of thin columns and a thick pillar was more accurate than the corresponding parameter obtained when leaves were modeled using several thin columns. Hence, I conclude that modeling roadside trees in a more realistic manner improves the accuracy of path loss prediction. Also, the absolute value of the mean error and the standard deviation are observed to decrease when modeling the roadside tree in a more realistic manner. The reason for the increased accuracy (increased predicted path loss) is due to the reduced number of multipath, which is analyzed in Section 3.4.2. Additionally, Fig. 3.3 shows the simulation accuracy changes according to the maximum number of reflection, diffraction, and the relative permittivity of the buildings used in the ray tracing simulation. It can be seen that the RMSE is distinctly low when the roadside tree is modeled even if the parameter changes. In addition, the order of the accuracy of each modeling method does not change according to parameters.

### 3.4.2 Multipath Component Analysis

The difference in path loss prediction accuracy is a result of the differing number of multipath caused by the inclusion of roadside tree models, and the tree modeling method used in the simulation. Table 3.2 shows the predicted number of rays. Since rays with low power have little effect on received signal strength, it is reasonable to count only those rays that exceed the appropriate threshold. The results after setting the threshold to $-140$ dB similarly to [42] and counting only the number of ray exceeding the threshold are shown in Table 3.2. In Table 3.2, the number of ray is smaller for cases where roadside trees are modeled than it is when only building models are included. The reason for the reduced number of rays is attributed to the strong transmission loss which occurred when passing through a roadside tree. Reduced multipath numbers simulate actual propagation channels better than conventional methods that use only building data.

The results of the number of clusters analysis of the received signal in the measurement area, presented in [36], support the above explanation. From the analysis detailed in [36], the value corresponding to 50% of clusters is 2.2, which is similar to

2, the median value of the number of multipath obtained by ray tracing simulations that include roadside tree models. In contrast, the difference between the number of clusters measured by experiment and the number of paths predicted by simulations using only building data is more significant. Fig. 3.4(a), (b), and (c) show the comparison of the results of channel modeling for cases where roadside tree models were included and excluded from the ray tracing simulation. As seen in Table 3.2, the number of

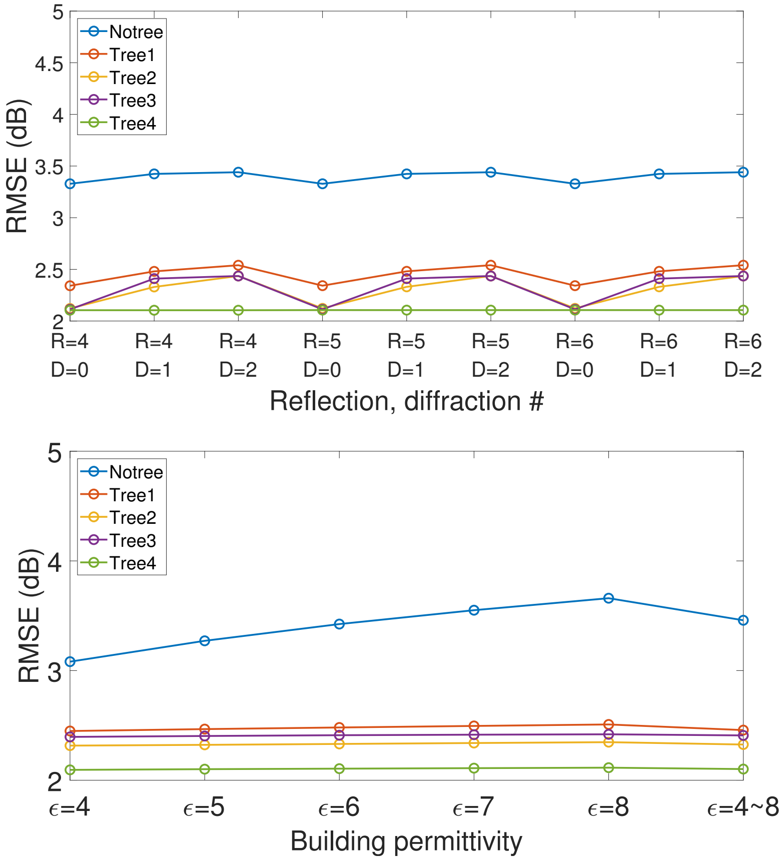

Figure 3.3: RMSE performance change with variation of ray tracing simulation parameter (a) RMSE change according to the maximum number of reflections and the number of vertical diffractions. (b) change of RMSE according to the relative permittivity of the buildings in ray tracing simulation.

Table 3.2: Channel prediction using ray tracing simulation

| | **Only building** | **Tree1** | **Tree2** | **Tree3** | **Tree4** |
|---|---|---|---|---|---|
| RMSE | 3.42 dB | 2.48 dB | 2.33 dB | 2.41 dB | 2.11 dB |
| Mean error | -3.10 dB | -1.87 dB | -1.60 dB | -1.81 dB | -1.42 dB |
| Std. dev. of error | 1.76 dB | 1.70 dB | 1.62 dB | 1.66 dB | 1.52 dB |
| # of cluster (median) | 7 | 5 | 4 | 4 | 2 |

paths is reduced with the inclusion of a roadside tree model.

The results of comparing cumulative distribution function(CDF) about the number of multipath clusters extracted from the received signal at each measurement point and about the number of rays generated in ray tracing simulation are shown in Fig. 3.4(d). For CDF generation, ray tracing simulation was performed at various locations near the measurement point. As in the case of comparing the median values of the number of clusters at each point, the order in which the number of clusters best matches the actual measurement results is consistent with the order of highest path loss prediction accuracy. As each simulated ray would represent a cluster of actual paths, the fact that the number of clusters recorded in measurement data is similar to the number of paths obtained from ray tracing simulation indicates that the inclusion of roadside tree models produces more realistic multipath channel behavior. In addition, more complex and realistic roadside tree models result in fewer multipaths and higher path loss accuracy. Thus, I conclude that modeling roadside trees as realistically as possible improves the accuracy of the simulation. Additionally, Fig. 3.4(e) compares the root mean square(RMS) delay spread. The tree modeling method is the Tree4, in which the number of clusters is most similar to the actual measurement results. As with the number of clusters, the CDF of the RMS delay spread is closer to the actual measurement results, compared to the case where only the buildings are present.

Collectively, the results show that considering the roadside trees for ray tracing simulation improves accuracy regarding the multipath component.

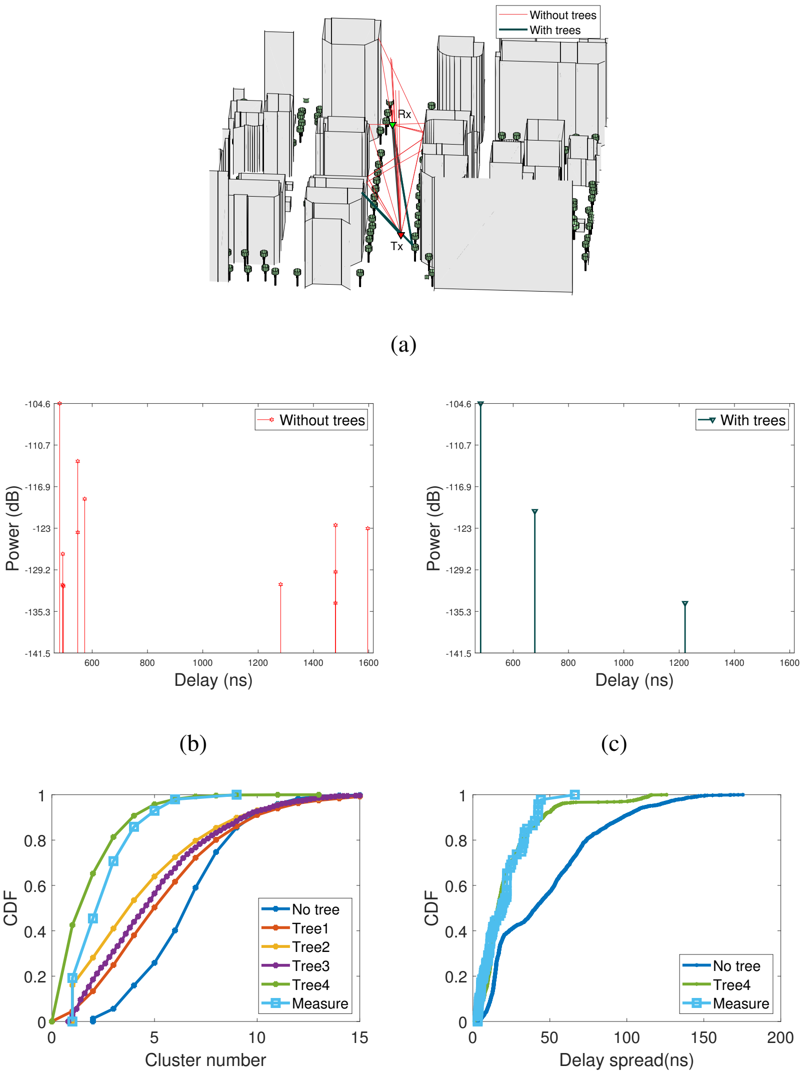

(a)

(b)

(c)

(d)

(e)

Figure 3.4: Effects of roadside tree modeling on ray tracing simulation. (a) Change in number of paths depending on presence or absence of roadside trees. (b) Power delay profile when only buildings exist. (c) Power delay profile when roadside tree (Tree4) exist. (d) The number of clusters by modeling method (e) Comparison of RMS delay spread with and without roadside tree modeling.

Table 3.3: Channel prediction using ray tracing simulation

| | **MJ (Building)** | **MJ (Tree4)** | **HN (Building)** | **HN (Tree4)** |
|---|---|---|---|---|
| RMSE - LOS (PL) | 10.3 dB | 5.4 dB | 4.0 dB | 1.7 dB |
| RMSE - NLOS (PL) | 11.0 dB | 10.5 dB | 6.3 dB | 5.3 dB |
| RMSE - LOS (Delay) | 7.2 ns | 1.0 ns | 19 ns | 2.4 ns |
| RMSE - NLOS (Delay) | 1.4 ns | 0.6 ns | 92 ns | 14 ns |

In addition, the results of comparing path loss and RMS delay in Moonjeong (MJ) and Hanam (HN) are shown in Table 3.3. The 28GHz band channel measurements in MJ and HN were carried out with systems similar to those mentioned earlier in this chapter. We can confirm that the ray tracing simulation has higher accuracy when the Tree 4 is modelled compared to when only building is modelled.

### 3.4.3 Computational Complexity

More complex roadside tree models increase the number of computations required for ray tracing simulations. When only buildings were modeled, 6589 structures were generated and the simulation took 891 seconds. In contrast, 21756 structures were generated and the simulation took 3008 seconds using the fourth method detailed in this chapter. As the number of structures increase, more reflection and diffraction points are generated, and a large amount of calculation is required. However, in spite of this increased computational complexity, there is no dramatic difference in prediction accuracy. Since ray tracing simulation is typically implemented to reduce the cost and time required for channel characterization in comparison to actual measurements, I conclude that a simple cylindrical model is sufficient in situations where speed is important, and the complexity of the tree modeling method should be increased for situations where greater accuracy is required.

## 3.5 Summary

In this study, I analyzed the effects of including roadside tree models in simulating wireless channel behavior using 3D ray tracing. I used a database of roadside trees recorded through the analysis of street view and satellite map data, in combination with a commercially available building database, to perform ray tracing simulations. I studied the influence of a variety of roadside tree models using path loss and multipath component analysis. The improved prediction accuracy highlighted the influence of the inclusion of roadside trees in modeling millimeter wave channels. I also noted differences in the accuracy of the predicted channel depending on the tree modeling method.

# Chapter 4

# Path Loss Exponent Prediction for Outdoor Millimeter Wave Channels through Deep Learning

## 4.1 Motivation

Recently, a 5G communication system using a millimeter-wave band to process massive data traffic has been receiving a great deal of attention. The millimeter-wave band has a broader bandwidth than the 6 GHz band used in conventional communication systems, and it is easy to allocate continuous frequency resources, which can increase the capacity of the communication system. However, the millimeter-wave band is known to be strongly influenced by obstacles, atmospheric conditions, and rainfall due to propagation loss [31, 32]. Therefore, it has different propagation characteristics than the sub-6 GHz band, and high path loss occurs at the same distance. Thus, more accurate channel information is required for base station placement and cell planning.

Propagation phenomena in mobile communication environment are very complicated due to reflection, transmission, diffraction, and dispersion, and expressing them using analytical tools (e.g., mathematical modeling) has limitations. Propagation phenomena vary depending on the carrier frequency, bandwidth, propagation environment (indoor/outdoor, urban/residential area, terrain, building material structure, etc.). Existing channel models use the stochastic or deterministic model to represent radio wave propagation phenomena. The former uses model parameters that are statistically represented through repeated measurements in each radio environment, and the latter uses a method like a ray tracing algorithm that expresses the propagation environment by ray paths.

The statistical method is expressed as a probability function of the parameters that can represent the propagation environment. The stochastic model has the benefit that it can estimate the propagation characteristics quickly even over a large area because the amount of computation required is small. However, it has low accuracy because it does not consider environmental characteristics.

On the other hand, the ray tracing method has much higher accuracy than the stochastic model because it considers the environmental characteristics of a specific area. However, the ray tracing method has very high computational complexity because each ray used for propagation prediction must be tracked.

In the existing 3G and 4G communication systems, the computational complexity, inference time, and accuracy of the channel models were not the biggest issue because there was little need for an accurate and rapid prediction of the optimum location of the base station. However, with the arrival of 5G communication and the need for smaller coverage and moving base stations like drone-base stations, the task of finding the optimal location of the base station is common and must be done in a very short time.

[44, 45, 46] used machine learning methods (feedforward net, random forest) to predict the path-loss exponent. However, because the training was only based on experimental results, the generality of neural networks is insufficient. In addition, latitude, longitude, and altitude are used as input parameters, so the specificity of the environment is ambiguously represented in the neural network. [47] uses various data obtained by ray tracing to predict time series of the received signal strength, but it does not predict the path loss exponent in a specific environment.

In this paper, to combine the advantages of deterministic and stochastic modeling, I propose an algorithm that uses deep learning method which can maintain both the advantages of the accuracy of the ray tracing model and short inference time of the stochastic model. I analyzed the performance changes caused by selecting the hyperparameters used for training. Moreover, to analyze whether the prediction of the trained neural network is affected by the environment, I investigated the performance difference for changes in the number of buildings and average distance from the transmitter.

## 4.2 Processing Training Data

For the neural network to recognize the characteristic of the building and the terrain of the map, the input data must represent the environment properly.

In this section, I describe input data used in neural networks and the process of obtaining output data, i.e., the path loss exponent. The process of transforming the map around the area of interest into an image for the input of the neural network is also described. The generated input and output data are used for training and testing the neural network.

### 4.2.1 Map transformation process

In this chapter, the map around the area of interest is converted into an image for the neural network and used as input data. The map of the area of interest consists of the terrain data of the area, as well as the shape and height of the building. An example of a three-dimensional map is shown in Fig. 4.1.

Because propagation characteristics vary with the building, terrain, and transmitter height and location in the area, it is essential to adequately represent a parameter in the two-dimensional image. Since I always set the position of the transmitter to the center (0,0) of the area of interest, only the height of the building, the terrain, and the height of the transmitter are represented in the input image. In this chapter, the color corresponding to each pixel of the two-dimensional image was used to convert the three-dimensional map data into two-dimensional. Each pixel of color image data has a value corresponding to red, green, and blue. In this study, the value corresponding to the height of the building is represented in red as follows:

$$R = \frac{H_B}{40} \times 255 \tag{4.1}$$

where $R$ is the color value of red and $H_B$ is the height ($m$) of the building. Since the value corresponding to each color should have a number between 0 and 255, the maximum value of the calculated value is normalized to be 255. Also, since almost all buildings in Seoul used as the training and test data in this study have a height of less than 40 m, normalization was performed by dividing the height of all buildings by 40 m. An example of such a red colored map is shown in Fig. 4.2(a).

In this study, I mixed the height of the transmitter and the terrain data of the building adequately and represented this value in green. Instead of defining the height of

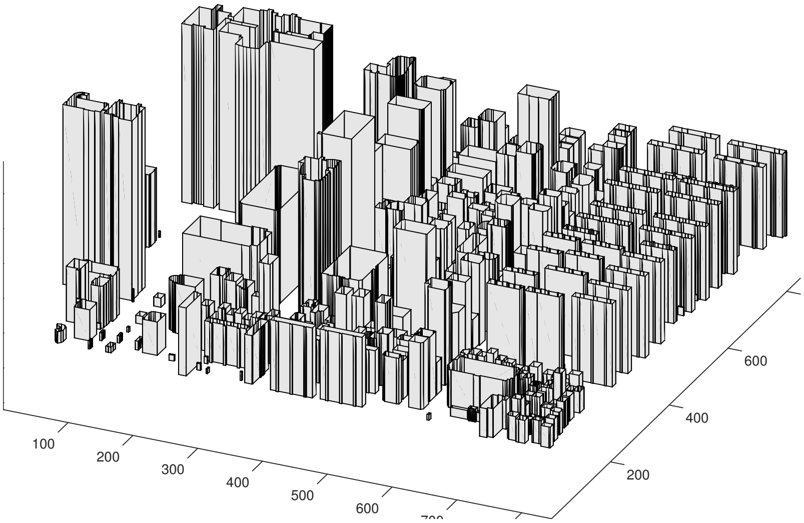

Figure 4.1: Three-dimensional building map example.

the transmitter and the terrain data of the building in color separately, there are two reasons for mixing the height of the transmitter and the terrain data of the building. One reason is that I fixed the position of the transmitter at (0, 0) in this study. The convolutional neural network (CNN) technique, which is a deep learning method used in this study, observes multiple pixels at the same time and extracts characteristics from the images instead of observing the individual pixels of the image. Neural networks cannot correctly infer properties if only the color changes at a fixed position (0, 0). Therefore, to represent the height of the transmitter and terrain data simultaneously, I defined new a parameter that combines the height of the transmitter with the terrain data of the building so that the neural network can recognize it properly. Another reason is that the height of the transmitter and the terrain data of the building affect the propagation characteristic of the radio in combination. The higher height of the transmitter and the lower height of the building terrain yields the greater height difference between them. Since the high relative height of the transmitter increases the probability of line of sight, it is reflected in green so that the image can predict the propagation characteristics well. Transmitter height and terrain data are indicated in green as follows:

$$G = \frac{H_{T0} - H_{G0}}{40} \times 255 \tag{4.2}$$

where $G$ is the color value of green, $H_{T0}$ is the height of the transmitter from sea level, and $H_{G0}$ is the height of the ground from sea level. An example of a map reflecting the green color is shown in Fig. 4.2(b). The maps reflecting the red and green colors are combined as a color image as shown in Fig. 4.2(c). I used this color image as input data for the neural network.

### 4.2.2 Generating path loss exponent for output data

This section describes how to generate the path loss exponent, which will be used as the output data of the neural network. When the map of the area of interest is entered

(a)

(b)

(c)

Figure 4.2: Examples of image sets used as learning data. Transmitter height, ground height, and building height are represented in each color map.

into the neural network, the average path loss exponent should be generated as the output. The path loss exponent can be obtained based on the received signal strength (RSS) at each receiving point in the area. Ideally, it is best to use experiment-based measurement data for all maps used in training, validation, and testing and then use this as output data. However, it is impossible to obtain millimeter-wave band channel data for a substantial number of areas. Therefore, in this chapter, I used the ray tracing simulator which applies the vertical plane launch (VPL) method, one of the ray tracing techniques, to obtain RSS values in various regions. The VPL method was first proposed in 1998 by Liang and Bertoni to simulate three-dimensional radio propagation channels efficiently [38]. The ray tracing method, which predicts propagation characteristics using building shape, terrain data, and transceiver characteristics, has the advantage of higher accuracy than the existing stochastic model. [39, 40, 48] confirmed that the RSS obtained through the VPL technique is very similar to the actual measurement results.

The ray tracing simulator used in this study traces the ray path by dividing the space into vertical and horizontal planes. The simulator first emits rays in the horizontal direction, as in the case of the two-dimensional pincushion method, as shown in Fig. 4.3. This ray represents a vertical plane containing all elevation angles originating from the transmitter. The vertical plane is divided into a plane that passes through the wall when facing it or a plane that diffracts or reflects in the direction of the specular reflection. After considering the propagation of the vertical plane in the horizontal area, the path between the transmitter and the receiver is calculated.

A ray is considered to reach the receiver when it crosses a capture circle at the reception location. When the ray reaches the receiver, the path and all reflection and diffraction coefficients are calculated. Because the simulator emits rays at all azimuth and elevation angles, the computation time exponentially increases with map area, angular resolution, and so on. Also, the roadside tree modeling was considered to improve the accuracy of the Ray tracing simulation.

## 4.3 Neural Network Structure

This section describes the structure of CNN, which is a neural network used in the proposed technique. The neural network is a machine learning method that can learn the characteristic of data through hierarchical abstraction at various levels using a computational model composed of several layers of nonlinear modules. Unlike the feature extraction step in the existing data-based diagnostic method, it is possible to learn the optimal hierarchical features directly from the data. Also, the neural network shows high performance in various fields such as object recognition. CNN is a deep learning technique that improves performance in computer vision and image recognition. As shown in Fig. 4.4, it consists of a convolutional layer, a pooling layer, a nonlinear activation function, and a fully-connected layer. The CNN model is characterized by local connectivity and weight sharing, and it is a neural network model that significantly reduces the number of weights compared to the fully-connected neural network model. In this study, I used a converted two-dimensional image for input of CNN. The map of 1 km by 1 km used for input is converted into an image of 300 × 300 pixels by the method described in Section II. The output is the path loss exponent obtained from ray

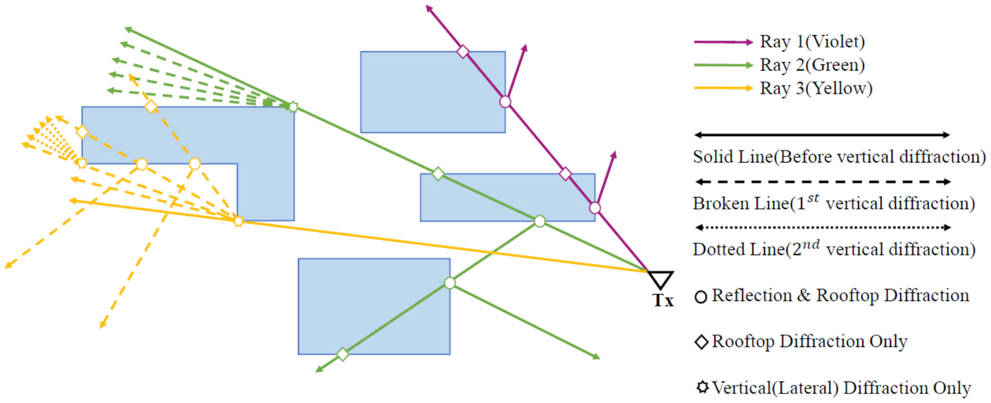

Figure 4.3: Computation of three-dimensional ray tracing in horizontal space.

tracing simulation.

## 4.4 Numericl Result Analysis

### 4.4.1 Simulation parameters

I obtained Geographic Information System (GIS) data from the National Geographic Information Institute, a subordinate organization of the Ministry of Land, Infrastructure, and Transport, South Korea to simulate the propagation channels in various environments. I divided the obtained maps of Seoul into 1 km by 1 km units and used them as input data. A total of 644 maps were generated. The process of dividing the map is shown in Fig. 4.5. I transformed individual maps to the two-dimensional image according to the transmitter's height (5, 10, 15, 20, 25 m). Therefore, the number of total maps became 3220. Also, each map was copied and rotated from 0 to 180 degrees by 1 degree to increase the generality of the neural network. Thus, I used a total of 576,720 images for training and testing neural networks. Propagation channel prediction was carried out in the 28 GHz millimeter-wave band. The simulation parameters and ray tracing modeling parameters are shown in Table 4.1. For the training of neural networks, I classified the data into training, validation, and test set. Each set used 70%,

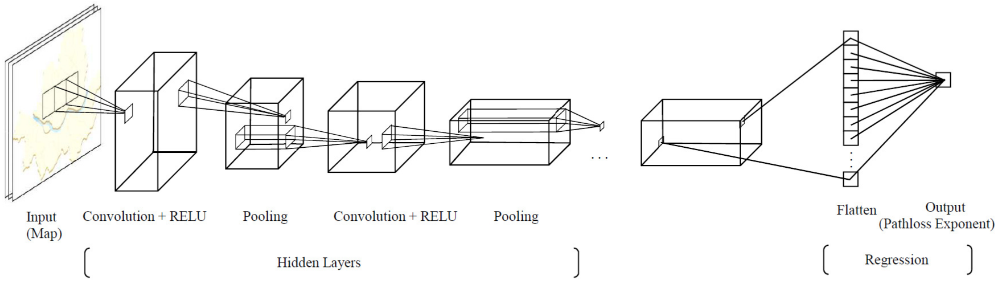

Figure 4.4: Structure of a convolutional neural network. Map data is used as input, and path loss exponent is used as output.

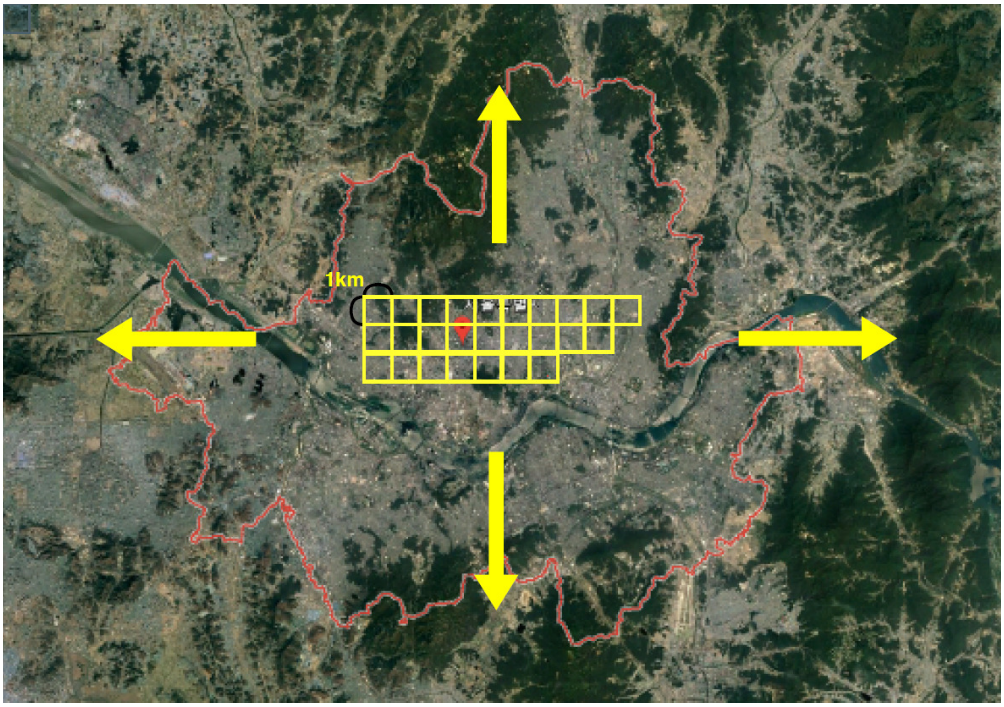

Figure 4.5: The process of dividing Seoul into square shaped tiles. A total of 644 tiles are created.

15%, and 15% of the total data, respectively.

### 4.4.2 Optimal hyperparameter selection

In this study, I analyzed how the prediction performance changed according to the hyperparameter change. The relative root mean square error (RMSE) for each hyperparameter is shown in Table 4.2. Table 4.2 shows the prediction performance according to the learning rate and layer number change.

If the learning rate is not properly selected, the validation loss increases. Therefore, the learning rate was chosen as an appropriate value so that the validation loss does not diverge. As a result of testing several hyperparameters, number of layers and learning rates with optimal performance are 6 and $5 \times 10^{-4}$, respectively. In addition, we compared the experimental results with the predicted results to confirm the performance

Table 4.1: System Parameters

| **Parameter** | **Value** |
|---|---|
| Center frequency | 28 GHz |
| Transmitter height | 5, 10, 15, 20, 25 m |
| Maximum number of reflection | 4 |
| Maximum number of vertical diffraction | 1 |
| Maximum number of horizontal diffraction | 4 |
| Relative permittivity of building wall | 6 |
| Ray shooting angle resolution | 0.1 ° |
| Learning rate drop factor | 0.1 |
| Learning rate drop period | 20 |
| Filter size for each layer | 3×3 |
| Number of filters for each layer | 15 |
| Pooling method | Average pooling |

of the proposed algorithm when using optimal hyperparameter. Table 4.3 compares measured and predicted results at Moonjeong (MJ), Hanam (HN), and Daejeon (DJ). The RMS delay was also trained to the CNN structure and compared with the experimental results. Both LOS and NLOS case, proposed method shows small errors when compared with the measured results.

### 4.4.3 Relationship between environment and prediction accuracy

In this study, I analyzed whether the relative error of the path loss exponent prediction changes according to the target environment. I examined whether the relative

Table 4.2: Hyperparameter vs Prediction error (%)

| **Learning rate** | **2 Layers** | **4 Layers** | **6 Layers** |
|---|---|---|---|
| $10^{-6}$ | 48.1 | 38.6 | 19.7 |
| $10^{-5}$ | 29.1 | 18.4 | 15.4 |
| $5 \times 10^{-5}$ | 17.9 | 15.1 | 11.9 |
| $10^{-4}$ | 15.9 | 14.7 | 11.8 |
| $2 \times 10^{-4}$ | 17.1 | 12.7 | 10.1 |
| $5 \times 10^{-4}$ | 11.1 | 12.9 | 9.71 |
| $10^{-3}$ | Inf | $5.95 \times 10^7$ | 10.2 |

Table 4.3: PLE prediction using ray tracing simulation

|  | **LOS PLE** | **LOS RMS delay** | **NLOS PLE** | **NLOS RMS delay** |
|---|---|---|---|---|
| MJ | 6.8 % | 13,2 % | 15 % | 19 % |
| HN | 15.2 % | 35 % | 23 % | 10 % |
| DJ | 2.5 % | 34 % | 22 % | 28 % |

prediction errors change as the number of buildings around the area of interest and the average distance of buildings from the transmitter change. Fig. 4.6(a) shows the relationship between the number of buildings and the relative prediction error of the path loss exponent. Even though the number of buildings increases, the prediction error of the path loss exponent does not increase, and the correlation between the two variables is also shallow. Therefore, I conclude that even if the number of buildings is changed, the proposed algorithm does not show a difference in prediction performance. In Fig. 4.6(b), I analyzed whether the average distance of buildings from the transmitter is correlated with the prediction error of the path loss exponent. It can be seen that the prediction error of the path loss exponent does not increase even if the distance from the transmitter increases and the correlation between the two parameters is low. Therefore, I conclude that the average distance between the transmitter and the building as well as the number of buildings does not affect the prediction error. In short, I conclude that the prediction error does not undergo serious changes depending on the environments.

## 4.5 Summary

In this chapter, I proposed a new algorithm to predict the path loss exponent of outdoor millimeter-wave band channel through deep learning. A three-dimensional radio ray tracing tool was used to generate the wireless channel data to train the path loss exponent on the neural network. After training the neural network with the channel data obtained from various environments, I evaluated the prediction performance of the neural network for the test data set. I obtained the optimal hyperparameter for the prediction of the path loss exponent. Also, I showed that the prediction performance does not show a significant difference with the number of buildings in the environment or the average distance of buildings from the transmitter. If I use the results presented in this study for path loss exponent or wireless coverage prediction, I will be able to obtain path loss exponent and wireless coverage in a short time for various areas.

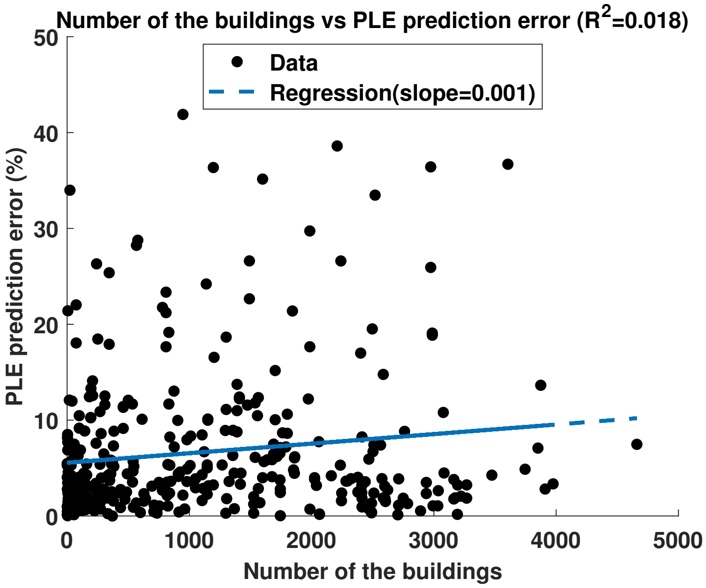

(a)

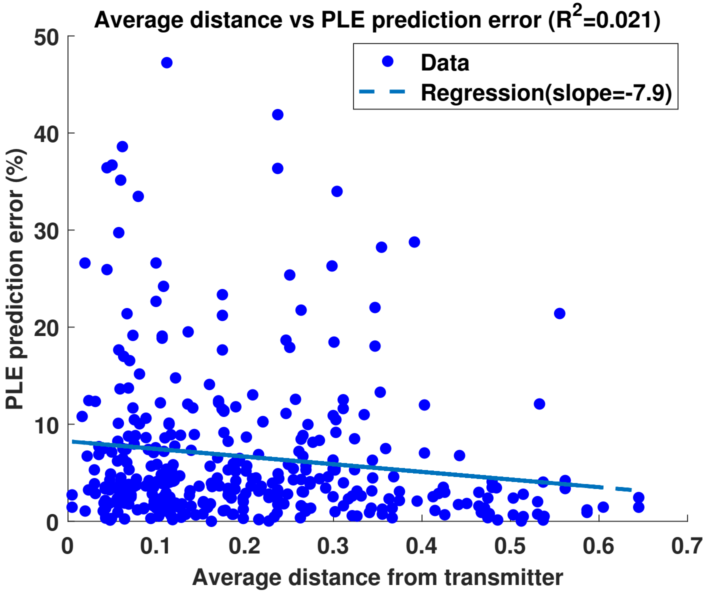

(b)

Figure 4.6: Analysis of path loss exponent (PLE) prediction performance change according to environment. Even if the environment changes, the prediction performance is almost unchanged.

# Chapter 5

# Conclusion

In this thesis, I solved the major problems in 5G through the following research. First, I developed an efficient and robust DP detection scheme for indoor positioning based on wireless communication systems. The motivation was to perform accurate ranging even in an environment where obstacles block the line-of-sight. The proposed method was developed on the basis of interference cancellation and an enhanced path detector. By subtracting the interference from the received signal, low power DP was distinguished from adjacent paths. An enhanced path detector was proposed independently of the interference cancellation method, and the results of both methods were employed together to detect the DP. The simulation results show that the ranging performance of the proposed algorithm tested in various environments is superior to the conventional methods. When there are many obstacles, the performance difference compared with the existing method is particularly large. I also investigated the distribution of the error by fitting it to various distributions. The fitting results obtained through the K–S test show that the distribution of errors is similar to a lognormal distribution. By using the proposed algorithm and error distribution model for ranging, it is expected that the positioning performance will be greatly improved. Next, I analyzed the effects of including roadside tree models in simulating wireless channel behavior using 3D ray tracing. I used a database of roadside trees recorded through the analysis of street view and satellite map data, in combination with a commercially available building database, to perform ray tracing simulations. I studied the influence of a variety of roadside tree models using path loss and multipath component analysis. The improved prediction accuracy highlighted the influence of the inclusion of roadside trees in modeling millimeter wave channels. I also noted differences in the accuracy of the predicted channel depending on the tree modeling method. Finally, I proposed a new algorithm to predict the path loss exponent of outdoor millimeter-wave band channel through deep learning. A three-dimensional radio ray tracing tool was used to generate the wireless channel data to train the path loss exponent on the neural network. After training the neural network with the channel data obtained from various environments, I evaluated the prediction performance of the neural network for the test data set. I obtained the optimal hyperparameter for the prediction of the path loss exponent. Also, I showed that the prediction performance does not show a significant difference with the number of buildings in the environment or the average distance of buildings from the transmitter. If I use the results presented in this study for path loss exponent or wireless coverage prediction, I will be able to obtain path loss exponent and wireless coverage in a short time for various areas.

# Bibliography

[1] Y. Guo, “Wavelet packet transform-based time of arrival estimation method for orthogonal frequency division multiplexing ultra-wideband signal,” *IET Sci., Meas. Technol.,* vol. 9, no. 3, pp. 344–350, Apr. 2015.

[2] W. Wang, T. Jost, C. Gentner, S. Zhang, and A. Dammann, “A semiblind tracking algorithm for joint communication and ranging with OFDM signals,” *IEEE Trans. Veh. Technol.*, vol. 65, no. 7, pp. 5237–5250, Jul. 2016.

[3] M. Noschese, F. Babich, M. Comisso, C. Marshall, and M. Driusso, “A low-complexity approach for time of arrival estimation in OFDM systems,” in *Int. Symp. Wireless Comm. Sys. (ISWCS),* Aug. 2017, pp. 128–133.

[4] Y. Liu et al., “High-Robustness and Low-Complexity Joint Estimation of TOAs and CFOs for Multiuser SIMO OFDM Systems,” *IEEE Trans. Veh. Technol.,* vol. 67, no. 8, pp. 7739–7743, Aug. 2018.

[5] L. Jing, T. Pedersen, and B. Fleury, “Direct ranging in multi-path channels using OFDM pilot signals,” in *Sig. Proc. Advances in Wireless Com. (SPAWC)*, Jun. 2014, pp. 150–154.

[6] N. Salman, N. Alsindi, L. Mihaylova, and A. H. Kemp, “Super resolution WiFi indoor localization and tracking,” in *Proc. Sensor Data Fusion: Trends, Solut., Appl. (SDF),* Oct. 2014, pp. 1–5.

[7] A. Makki, A. Siddig, M. M. Saad, J. R. Cavallaro, and C. J. Bleakley, "High-resolution time of arrival estimation for OFDM-based transceivers," *Electron. Lett.,* vol. 51, no. 3, pp. 294–296, Feb. 2015.

[8] O. Bialer, D. Raphaeli, A. J. Weiss, "Robust time-of-arrival estimation in multipath channels with OFDM signals," in *Europ. Sig. Process. Conf. (EUSIPCO),* Aug. 2017, pp. 2724–2728.

[9] W. Xu, M. Huang, C. Zhu, and A. Dammann, "Maximum likelihood TOA and OTDOA estimation with first arriving path detection for 3GPP LTE system," *Trans. Emerg. Telecommun. Technol.,* vol. 27, no. 3, pp. 339–356, Mar. 2016.

[10] T. E. Abrudan, A. Haghparast and V. Koivunen, "Time Synchronization and Ranging in OFDM Systems Using Time-Reversal," *IEEE Trans. Instrum. Meas.,* vol. 62, no. 12, pp. 3276–3290, Dec. 2013.

[11] A. Makki, A. Siddig, and C. J. Bleakley, "Robust high resolution time of arrival estimation for indoor wlan ranging," *IEEE Trans. Instrum. Meas.,* vol. 66, no. 10, pp. 2703–2710, Jun. 2017.

[12] F. Babich, M. Noschese, C. Marshall, and M. Driusso, "A simple method for ToA estimation in OFDM systems," in *Europ. Nav. Conf. (ENC),* May 2017, pp. 305–310.

[13] T. Xie, C. Zhang, Y. Li, H. Jiang and Z. Wang, "An enhanced TDoA approach handling multipath interference in Wi-Fi based indoor localization systems," in *IEEE Int. Midwest Symp.Circuits Syst. (MWSCAS),* Aug. 2017, pp. 160–163.

[14] S. Hu, A. Berg, X. Li, and F. Rusek, "Improving the performance of OTDOA based positioning in NB-IoT systems," in *Proc. IEEE Global Commun. Conf. (GLOBECOM),* Dec. 2017, pp. 1–7.

[15] Z. He, Y. Ma, and R. Tafazolli, “Improved high resolution ToA estimation for OFDM-WLAN based indoor ranging,” *IEEE Wireless Commun. Lett.,* vol. 2, no. 2, pp. 163–166, Apr. 2013.

[16] A. Makki, A. Siddig, M. Saad, J. Cavallaro, and C. Bleakley, “Indoor localization using 802.11 time differences of arrival,” *IEEE Trans. Instrum. Meas.,* vol. 65, no. 3, pp. 614–623, Mar. 2015.

[17] J. Yang, X. Wang, S. Park, and H. Kim, “Direct path detection using multipath interference cancellation for communication-based positioning system,” *EURASIP J. Adv. Signal Process.,* vol. 2012, no. 188, pp. 1–18, Aug. 2012.

[18] J. Yang, X. Wang, S. I. Park and H. M. Kim, “Optimal direct path detection for positioning with communication signals in indoor environments,” in *Proc. IEEE Int. Conf. Commun.,* Jun. 2012, pp. 4798–4802.

[19] K. Chetty, G. Smith, and K. Woodbridge, “Through-the-wall sensing of personnel using passive bistatic WiFi radar at standoff distances,” *IEEE Trans. Geosci. Remote Sens.,* vol. 50, no. 4, pp. 1218–1226, Apr. 2012.

[20] H. Minn, D. I. Kim, and V. K. Bhargava, “A reduced complexity channel estimation for OFDM systems with transmit diversity in mobile wireless channels,” *IEEE Trans. Commun.,* vol. 50, no. 5, pp. 799–807, May 2002.

[21] J.-J. van de Beek, O. Edfors, M. Sandell, S. K. Wilson, and P. O. Borjesson, “On channel estimation in OFDM systems,” in *Proc. IEEE 45th Vehicular Technology Conf.,* Jul. 1995, pp. 815–819.

[22] A. Awoseyila, C. Kasparis, and B. G. Evans, “Improved preamble-aided timing estimation for OFDM systems,” *IEEE Commun. Lett.,* vol. 12, no. 11, pp. 825–827, Nov. 2008.

[23] De Miguel, G., Besada, J.A., Casar, J.R.: "Probability of false alarm of CA-CFAR detector in Weibull clutter," *Electron. Lett.,* vol. 34, no. 8, pp. 806–807, Apr. 1998.

[24] X. Chen and W. Chen, "Clutter reduction based on coefficient of variation in through-wall radar imaging," in *IEEE Radar Conf. (RADAR),* Apr./May. 2013, pp. 1–4.

[25] J.-H. Jung, J. Lee, J.-H. Lee, Y.-H. Kim, and S.-C. Kim, "Ray-tracing aided modeling of user-shadowing effects in indoor wireless channels," *IEEE Trans. Antennas Propag.,* vol. 62, no. 6, pp. 3412–3416, Jun. 2014.

[26] J. Nam-Ryul, et al., "Performance of Channel Prediction Using 3D Ray-tracing Scheme Compared to Conventional 2D Scheme," in *Asia-Pacific Conf. Comm.,* Aug./Sept. 2006, pp. 1–6.

[27] S. Chang and E. J. Powers, "Efficient frequency-offset estimation in OFDM-based WLAN systems," *IEE Electron. Lett.,* vol. 39, no. 21, pp.1554–1555, Oct. 2003

[28] J. Lee, Y. Kim, J. Lee, and S. Kim, "An efficient three-dimensional localization scheme using trilateration in wireless sensor networks," *IEEE Commun. Lett.,* vol. 18, no. 9, pp. 1591–1594, Sep. 2014.

[29] T. Van Haute et al., "Performance Analysis of Multiple Indoor Positioning Systems in a Healthcare Environment," *Int. J. Health Geograph.,* vol.15, no.7, pp. 1–15, Feb. 2016.

[30] D. E. Kline and D. A. Bender, "Maximum likelihood estimation for shifted Weibull and lognormal distributions," *Trans. ASAE,* vol. 33, no. 1, pp. 330–335, Jan. 1990.

[31] Y. Azar, G. N. Wong, K. Wang, R. Mayzus, J. K. Schulz, H. Zhao, F. Gutierrez, D. Hwang, and T. S. Rappaport, “28 GHz propagation measurements for outdoor cellular communications using steerable beam antennas in New York City,” in *Proc. IEEE Int. Conf. Commun.,* pp. 1–6, Jun. 2013.

[32] A. O. Kaya, D. Calin, and H. Viswanathan, “28 GHz and 3.5 GHz wireless channels: Fading delay and angular dispersion,” in *Proc. IEEE Glob. Commun. Conf.,* pp. 1–7, Dec. 2016.

[33] N. Leonor, R. Caldeirinha, T. Fernandes, D. Ferreira, and M. Sanchez, ”A 2D ray-tracing based model for micro- and millimeter-wave propagation through vegetation”, *IEEE Trans. Antennas Propag.,* vol. 62, no. 12, pp. 6443–6453, Dec. 2014.

[34] B. Goktepe, M. Peter, R.J. Weiler, and W. Keusgen, “The influence of street furniture and tree trunks in urban scenarios on ray tracing simulations in the millimeter wave band,” in *Proc. European Microwave Conf.,* pp. 195–198, Sep. 2015.

[35] J.-J. Park, J. Liang, J. Lee, H.-K. Kwon, M.-D. Kim, and B. Park, “Millimeter-wave channel model parameters for urban microcellular environment based on 28 and 38 GHz measurements” in *Proc. IEEE 27th Annu. Int. Symp. Pers. Indoor Mobile Radio Commun.,* pp. 1–5, Sep. 2016.

[36] J. Lee, J. Liang, M.-D. Kim, J.-J. Park, and B. Park, “Measurement-based propagation channel characteristics for millimeter-wave 5G Giga communication systems,” *ETRI J.,* vol. 38, no. 6, pp. 1–11, Sep. 2016.

[37] National Geographic Information Institute. “Space information Open platform Map service,” [online] Available at: http://map.vworld.kr/map/maps.do [11 Dec. 2017].

[38] G. Liang and H. L. Bertoni, “A new approach to 3-D ray tracing for propagation prediction in cities,” *IEEE Trans. Antennas Propagat.,* vol. 46, no. 6, pp. 853–863, Jun. 1998.

[39] J. H. Lee, J. S. Choi, J. Y. Lee and S. C. Kim, “28 GHz Millimeter-Wave Channel Models in Urban Microcell Environment Using Three-Dimensional Ray Tracing,” *IEEE Antennas and Wireless Propag. Lett* vol. 17, no. 3, pp. 426–429, Mar. 2018.

[40] J. H. Lee, J. S. Choi, and S. C. Kim, “Cell coverage analysis of 28 GHz millimeter wave in urban microcell environment using 3-D ray tracing,” *IEEE Trans. Antennas Propagat.,* vol. 66, no. 3, pp. 1479–1487, Mar. 2018

[41] M. A. Karam, A. K. Fung, and Y. M. M. Antar, “Electromagnetic wave scattering from some vegetation samples,” *IEEE Trans. Geosci. Remote Sensing.,* vol. 26, no.6, pp. 799–808, 1988.

[42] Z. Zhang, J. Ryu, S. Subramanian, and A. Sampath, “Coverage and channel characteristics of millimeter wave band using ray tracing,” in *Proc. IEEE Int. Conf. Commun. (ICC),* pp. 1380–1385, Jun. 2015.

[43] F. Mani, E. M. Vitucci, M. Barbiroli, F. Fuschini, V. Degli Esposti, M. Gan, C. Li, J. Zhao, Z. Zhong, “26GHz Ray-Tracing Pathloss Prediction in Outdoor Scenario in Presence of Vegetation,” in *Proc. EuCAP,* Apr. 2018.

[44] S.I. Popoola, E. Adetiba, A.A. Atayero, N. Faruk, C.T. Calafate, “Optimal model for path loss predictions using feed-forward neural networks,” *Cogent Eng., vol. 5,* Feb. 2018.

[45] B. J. Cavalcanti and G. A. Cavalcante, “A Hybrid Path Loss Prediction Model based on Artificial Neural Networks using Empirical Models for LTE And LTE-A at 800 MHz and 2600MHz,” *Journal of Microwaves, Optoelectronics and Electromagnetic Applications,* vol. 16, pp. 704-718, Sep. 2017.

[46] C. A. Oroza, Z. Zhang, T. Watteyne and S. D. Glaser, “A Machine-Learning-Based Connectivity Model for Complex Terrain Large-Scale Low-Power Wireless Deployments,” *IEEE Trans. on Cognitive Comm. and Network.,* vol. 3, no. 4, pp. 576-584, Dec. 2017.

[47] Yan Zhang, Jinxiao Wen, Guanshu Yang, Zunwen He, and Xinran Luo, “Air-to-Air Path Loss Prediction Based on Machine Learning Methods in Urban Environments,” *Wireless Comm. and Mobile Computing.,* vol. 2018, Jun. 2018.

[48] J. Y. Lee, J. H. Lee and S. C. Kim, “Improving the Accuracy of Millimeter-Wave Ray-Tracing Simulations by Modeling Roadside Trees,” *IEEE Antennas and Wireless Propagation Letters,* vol. 18, no. 1, pp. 162–166, Jan. 2019.

# 초록

최근, 급격히 늘어나는 데이터 트래픽을 대비하기 위하여 ITU-R에서는 5세대 이동통신 개념을 정립하고 요구사항을 정의하였다. 이에 맞추어 3GPP 단체는 5G 용도의 New radio (NR) 규격을 개발하였으며, 한국에서는 5G 시대가 열리게 되었다. 5G 이동 통신 시스템은 기존 4G까지의 이동통신 시스템과는 달리 초고속, 초저지연, 초 연결 특성을 가지며 IoT 등에 적극적으로 활용될 계획이다. 또한 초고속 통신을 위한 접근으로 5G에서는 millimeter-wave 대역을 사용할 계획이다. millimeter-wave 대역은 넓은 주파수 대역을 사용할 수 있기에 높은 전송률을 달성할 수 있다. 하지만 높은 경로손실, 회절에 의한 감쇄 등은 millimeter-wave 사용에 있어 큰 난제이다. millimeter-wave를 통신 시스템에서 활용하기 위해서는 전파(wave)의 전파(propagation)특성을 면밀히 연구할 필요가 있다. 특히 회절과 투과에 의한 감쇄가 매우 심한 millimeter-wave 특성을 반영하기 위해선 실외에 존재하는 다양한 장애물들이 millimeter-wave 전파 특성에 미치는 영향을 분석해야 한다. 또한 5G 시스템에서는 날이 갈수록 증가하는 트래픽을 감당하고, 재난 상황 등에 유연하게 대처하기 위하여 이동가능 기지국을 고려하고 있다. 드론과 같이 이동 가능한 기지국에서는 빠르고 정확한 채널 분석과 커버리지 예측이 필수적이다. 한편, 5G 시스템에서는 초 연결 특성과 함께 IoT 플랫폼을 적극적으로 활용할 계획이다. IoT 플랫폼의 실용성을 증가시키기 위해서는 다수의 기기에 대한 위치 추정이 필수적이다. 본 논문에서는 5G 시스템이 대면한 다양한 이슈를 해결하기 위한 기법을 제시한다. 우선 본 논문에서는 길가의 가로수가 광선 추적 시뮬레이션을 사용한 채널 모델링의 정확성에 미치는 영향을 분석하였다. 가로수는 전파를 투과, 반사 및 회절 시키는 물

체로 모델링 되었다. 논문에서는 가로수가 포함된 광선 추적 시뮬레이션의 결과가 기존 시뮬레이션 결과에 비하여 실험적으로 측정된 결과와 매우 유사하다는 점을 발견하였다. 다음으로는 딥러닝 기법을 통해 실외 밀리미터 파 대역 채널의 경로 손실 지수를 예측하기 위한 새로운 알고리즘을 제안한다. 제안된 알고리즘은 기존의 결정론적 채널 모델에 비해 추론 시간을 덜 필요로 한다는 장점이 있으며, 지형적 특성을 구체적으로 고려할 수 있다. 실외 밀리미터 파 채널의 경로 손실 지수를 생성하기 위해서는 광선 추적 시뮬레이션을 사용하였다. 또한, 생성된 경로 손실 지수로 합성 곱 신경망을 훈련시켰다. 제안된 방법의 성능을 평가하기 위해 건물의 밀도와 송신기로부터의 평균 거리와 같은 환경 특성의 영향과 하이퍼 파라미터의 영향을 분석했다. 마지막으로 OFDM 기반의 통신 시스템을 이용하여 위치 추정을 위한 거리측정 성능을 향상시키는 방법을 제안한다. 통신 시스템의 ToA 정보를 사용할 때 위치 추정에 있어 가장 어려운 측면은 직접경로가 장애물에 의해 차단될 때 직접 경로와 간접 경로 및 잡음을 구별하는 것이다. 본 논문에서는 간섭 제거와 향상된 경로 검출기의 결합으로 인접한 경로 들로부터의 간섭을 제거하고 저전력 DP를 검출한다. 제안된 방법은 802.11ac 환경에서 검증되었으며 기존 방법에 비해 성능이 향상되는 것을 확인하였다.

**주요어**: OFDM, 가로수, 경로손실 지수, 광선추적기법, 딥러닝, 밀리미터파, 위치추정, 직접경로, 채널 모델링

**학번**: 2013-20856